nature genetics

Article

https://doi.org/10.1038/s41588-024-01832-5

Condensin I folds the *Caenorhabditis elegans* genome

Received: 1 April 2022

Accepted: 13 June 2024

Published online: 22 July 2024

Check for updates

Moushumi Das[1,2], Jennifer I. Semple[1], Anja Haemmerli[1], Valeriia Volodkina[1,2], Janik Scotton[1], Todor Gitchev[1], Ahrmad Annan[1], Julie Campos[1], Cyril Statzer[3], Alexander Dakhovnik[3], Collin Y. Ewald[3], Julien Mozziconacci[4] & Peter Meister[1]

The structural maintenance of chromosome (SMC) complexes—cohesin and condensins—are crucial for chromosome separation and compaction during cell division. During the interphase, mammalian cohesins additionally fold the genome into loops and domains. Here we show that, in *Caenorhabditis elegans*, a species with holocentric chromosomes, condensin I is the primary, long-range loop extruder. The loss of condensin I and its X-specific variant, condensin I^{DC}, leads to genome-wide decompaction, chromosome mixing and disappearance of X-specific topologically associating domains, while reinforcing fine-scale epigenomic compartments. In addition, condensin I/I^{DC} inactivation led to the upregulation of X-linked genes and unveiled nuclear bodies grouping together binding sites for the X-targeting loading complex of condensin I^{DC}. *C. elegans* condensin I/I^{DC} thus uniquely organizes holocentric interphase chromosomes, akin to cohesin in mammals, as well as regulates X-chromosome gene expression.

Eukaryotic genomes undergo extensive folding during interphase while maintaining essential functions such as replication, transcription and repair[1–4]. In multicellular eukaryotes, the genome is organized across different scales. Long-range contacts between large megabase domains of two different types, A and B, create two compartments identified as eu- and heterochromatin, respectively[2]. Over shorter distances, chromosomes are folded into loops and topologically associating domains (TADs), insulated three-dimensional (3D) domains restricting enhancer action to specific promoters and increasing enhancer–promoter contact probability[5–10]. The formation of TADs is the result of chromatin loop extrusion activities of the structural maintenance of chromosome (SMC) complexes[11–18]. In mammals, cohesin is the major SMC loop extruder, interacting with oriented sequence elements bound by transcription factors such as CCCTC-binding factor (CTCF) to define boundaries between TADs[19–21].

Condensins, another conserved SMC complex, are essential for the compaction and mechanical rigidity of mitotic chromosomes[22]. They play a crucial role in chromosome compaction in budding yeast[23,24] and long-range organization into domains in fission yeast[25–27]. Two variants of condensin (I and II) are present in many species, including mammals and *Drosophila* spp.[22]. The presence of the condensin II SMC complex correlates with interphase 3D chromosome organization[28], most probably indirectly via its action in lengthwise compaction of chromosomes during mitosis, retained in subsequent interphases owing to the slow dynamics of long chromosomes. Species without condensin II therefore have more clustered centromeres and/or heterochromatin, whereas species with condensin II display chromosomal territories and poor centromeric clustering[28]. In mammals, condensin complexes are either excluded from the nucleus or fail to bind chromatin outside of mitosis[29,30]. Notably, *C. elegans* appears to be an exception to this rule, because at least one condensin complex is nuclear and active during interphase[31,32].

Like most animals, nematodes express homologs of cohesin, condensin I and II in somatic cells[33,34]. Two variants of the cohesin complex

[1]Cell Fate and Nuclear Organization, Institute of Cell Biology, University of Bern, Bern, Switzerland. [2]Graduate School for Cellular and Biomedical Sciences, University of Bern, Bern, Switzerland. [3]Eidgenössische Technische Hochschule Zürich, Department of Health Sciences and Technology, Institute of Translational Medicine, Schwerzenbach, Switzerland. [4]Laboratoire Structure et Instabilité des Génomes UMR 7196, Muséum National d'Histoire Naturelle, Paris, France. e-mail: peter.meister@unibe.ch

are present, distinguished by their kleisin subunits, COH-1 or SCC-1 (ref. 35) (Fig. 1a). Previous analysis[34] of knock-down phenotypes of the kleisins suggests a mitotic function for cohesin^{SCC-1} and nonmitotic functions for cohesin^{COH-1}. In addition, the two kleisins are differentially localized: SCC-1 is expressed in dividing cells, whereas COH-1 is present in most nuclei[34]. In the absence of cohesin SMC subunits, many cells undergo catastrophic mitosis during embryonic development[34,36,37], as well as defects in ribosomal DNA compaction[38], hindering further analysis of their interphasic function.

Nematode condensin I and II are essential for chromosome condensation during mitosis[33,39,40]. Deletions or knock-downs of most condensin subunits result in mitotic catastrophe in early embryos and nuclear defects in postembryonic lineages[41–43]. A third condensin, condensin I^{DC} (for dosage compensation) in which one condensin I SMC subunit, SMC-4, is replaced by DPY-27, localizes specifically to the X chromosome throughout the cell cycle in hermaphrodites. Specific X-chromosome targeting of condensin I^{DC} is achieved by the sex determination and dosage compensation (SDC) complex and a sequence motif called MEX (motif extraction) enriched on X chromosomes[44]. Binding of condensin I^{DC} in hermaphrodites leads to downregulation of X-linked gene transcription, compensating for the chromosomal imbalance between X chromosomes and autosomes. Structurally, loading of condensin I^{DC} leads to the formation of TADs and loops specific to the nematode X chromosome[45–47]. However, it remains unclear which SMC complexes fold the other chromosomes.

In the present study, we analyzed the role of the five major somatic SMC complexes in chromosome structure during interphase by inducing cleavage of these complexes in mostly postmitotic animals. Our results reveal that, in contrast to mammals, cohesins play a minor role in large-scale genome folding, whereas condensin I/I^{DC} is the primary loop extruder. Similar to cohesin loss of function in mammals, cleavage of condensin I/I^{DC} reinforces the epigenetic-driven compartmentalization and results in the loss of TADs on the X chromosome. Cleavage of condensin I/I^{DC} revealed the existence of an X-specific compartment enriched for the SDC complex, which we named SDC bodies. At the transcriptional level, cleavage of individual SMC complexes leads to moderate changes in gene expression, except for condensin I/I^{DC}, the cleavage of which results in a major upregulation of X-linked genes and reduced animal lifespan as a result of its function in dosage compensation. Our study highlights an unexpected function of condensin I in interphase genome folding in holocentric nematodes, with a major role in compartmentalization regulation and X-specific dosage compensation.

Results

To interrogate the functions of individual SMC complexes, we constructed strains in which kleisin subunits are modified using genome editing to include three cleavage sites for the tobacco etch virus (TEV) protease preceded by a single FLAG tag (Fig. 1a)[48]. We created cleavable COH-1 and SCC-1 kleisins for the two somatic cohesins and cleavable DPY-26 and KLE-2 kleisins for condensin I/I^{DC} and condensin II. Unless otherwise specified, experiments were carried out in animals by inducing SMC complex cleavage by activating TEV expression by a short (30-min) heat shock in the first larval stage (L1) where most cells are postmitotic, and collecting animals 19 h later at the third larval stage (L3), when the germline is still small.

Cohesin^{COH-1} and condensin I are the most abundant somatic SMCs

Under normal conditions, animals tolerated TEV-cut sites in kleisins without exhibiting any apparent phenotypes. A single FLAG tag was insufficient for kleisin detection by western blotting; hence we added two additional tags to enable detection, in otherwise identical strains. All kleisins were detected in the L3 stage whole-animal lysates using these triple FLAG strains (Fig. 1b and Supplementary Fig. 1a). COH-1, SCC-1 and DPY-26 were readily identifiable whereas the KLE-2 signal was faint, probably reflecting its lower or cell-type-specific expression. For cohesins, COH-1 was 6× more abundant than SCC-1, suggesting that most cohesin complexes are cohesin^{COH-1}, most probably because SCC-1 is expressed only in dividing cells[34]. Condensin I/I^{DC} kleisin DPY-26 was 90× more abundant than condensin II kleisin KLE-2; hence condensin I/I^{DC} is vastly predominant compared with condensin II (Fig. 1b and Supplementary Fig. 1a). In the absence of induction, and despite no detectable protease, a small proportion of both COH-1 and DPY-26 was cleaved. This had no discernible effect on the animals in both the single and the triple FLAG-tag strains. In particular, the well-characterized phenotype of short and fat (dumpy) animals that occurs on inactivation of condensin I^{DC} was never observed in the DPY-26 cleavage strain in the absence of TEV induction.

In vivo cleavage of kleisin subunits

Upon induction in the L1 stage, the protease was present at least until the L3 stage (Fig. 1b). The major condensin and cohesin kleisins COH-1 and DPY-26 were nearly fully cleaved (11% and 4% of uncut protein remaining; Fig. 1b and Supplementary Fig. 1b), whereas SCC-1 and KLE-2 full-length levels dropped by 32% or 50% (Fig. 1b and Supplementary Fig. 1b). This ineffective cleavage of SCC-1 and KLE-2 might be attributed to their higher turnover resulting from their mitotic functions: SCC-1 is known to be cleaved by separase during the transition from metaphase to anaphase[22] and at least one of the *Drosophila* condensin II subunits, CAP-H2, is degraded to facilitate chromosome decompaction during interphase[49,50]. Throughout all the experiments described below, we employed strains with a single FLAG tag.

Fig. 1 | Loss of cohesin^{SCC-1} and condensin II causes disruption in postembryonic vulval development and seam cell progression. **a**, Experimental approach to the functional analysis of SMC complexes in vivo (adapted from ref. 35). SMC complex protein composition for condensins and cohesins has a color code for kleisin that is maintained throughout all the figures. The cross symbol with a circle behind is the insertion site for the cleavage sequences of the TEV introduced by genome engineering. **b**, Comparison of individual kleisin expression levels and cleavage efficiency at the L3 stage upon TEV protease induction at the L1 stage. Quantification is from at least two experiments (Supplementary Fig. 1a). The expression of 3×FLAG-tagged kleisin is normalized to tubulin. The black arrowheads point to the expected sizes for the individual kleisins. **c**, Fluorescence in L3 stage animals expressing SMC-1::GFP, in the head (left) or the middle section of the animals (right). For each section, the left panel corresponds to control animals (no TEV protease) and the right shows animals in which TEV cleavage has been induced by heat shock. For the middle section, cell lineage is indicated by circles and autofluorescence of gut granules by stars. **d**, Phenotypic outcome 72 h post-induction of individual kleisin cleavage for the indicated SMC complexes and multiple SMC complexes. TEV control corresponds to an otherwise wild-type strain expressing the TEV protease. The color code is the same as in **a**. Experiments were carried out twice. **e**, Seam cell count per animal scored each day after kleisin cleavage induction. The color code is the same as in **a**. The midline, hinges and whiskers of the boxplot show the median, 25th and 75th quantiles, and the smallest/largest value no further than ±1.5× the interquartile range, respectively. The horizontal dashed lines denote the number of seam cells in an L1 stage (20) and in a fully developed adult (32). **f**, Lifespan analysis of hermaphrodites after kleisin cleavage at the L1 stage of the different indicated SMC complexes. Animals were transferred on day 1 of adulthood to plates with FUdR and scored automatically in the lifespan machine[101]. **g**, Lifespan analysis of hermaphrodites on auxin-mediated degradation of the condensin I^{DC} loader SDC-3, comparing animals without (control) and with (SDC-3 degradation) auxin. TEV control and condensin I/I^{DC} cleavage are the same as in **d** for the sake of comparison. **h**, Healthspan analysis of male animals in liquid medium on condensin I cleavage at first larval stage using a wMicroTrackerONE device. The error bars are ±s.d. from eight technical replicates, representing one of three independent biological repeats.

https://doi.org/10.1038/s41588-024-01832-5

Effect of cohesin kleisin cleavage on SMC-1 abundance

Previous studies have shown that COH-1 is expressed in most cells whereas SCC-1 is expressed in dividing ones[34]. To evaluate the cell-type-specific effect of kleisin cleavage on both cohesin complexes, we analyzed the distribution and expression levels of SMC-1, one of the two SMC proteins present in both cohesins, using an endogenously green fluorescent protein (GFP)-tagged protein[51]. SMC-1 is ubiquitously expressed at high levels in somatic cells, indicating that cohesins are

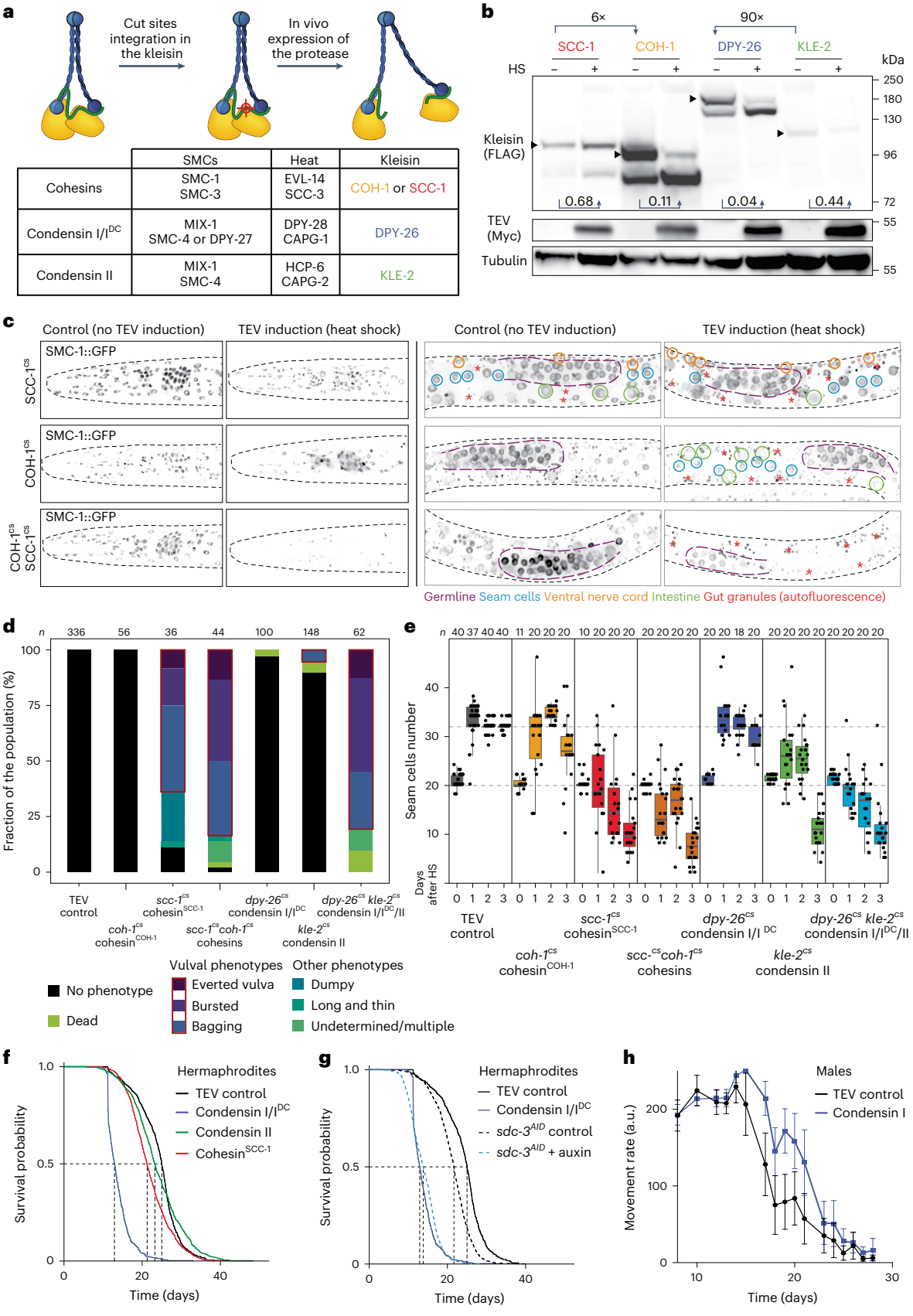

present in most, if not all, cells (Fig. 1c). In addition, SMC-1 is also present in the germline, where it is known to form different cohesin complexes with germline-specific kleisins (Fig. 1c, purple outline).

In control experiments (no TEV induction), SMC-1::GFP fluorescence remained comparable in the presence of cleavage sites in SCC-1, whereas it was lower when cleavage sites were introduced in COH-1 alone or in both kleisins simultaneously, indicating some degradation, although animals did not display any phenotype. To assess the effect of kleisin cleavage, we induced TEV expression at the L1 stage and imaged animals at the L3 stage. TEV induction alone had no impact on SMC-1 fluorescence levels (Supplementary Fig. 1c). When SCC-1 was cleaved, no major change in overall fluorescence occurred in somatic cells (Fig. 1c; quantified in Supplementary Fig. 1d). In contrast, when COH-1 was cleaved, many somatic nuclei completely lost fluorescence. In the central region of the animals (Fig. 1c, right panels), the remaining fluorescent nuclei were either intestinal nuclei or seam cell nuclei, two cell lineages that are mitotically active in overall postmitotic animals (Fig. 1c, green and blue circled nuclei). When both COH-1 and SCC-1 were cleaved simultaneously, SMC-1 fluorescence disappeared completely in the soma, whereas germline nuclei retained their fluorescence (Fig. 1c). Similar results were obtained when looking at the head of the animals (Fig. 1c, left panels; quantified in Supplementary Fig. 1d). When only COH-1 was cleaved, very few nuclei retained fluorescence and, although individual nuclei are difficult to identify in the head, these probably correspond to the handful of head neurons born postembryonically, which would therefore express the mitotic cohesin$^{SCC\text{-}1}$. Together, we conclude that cleavage of COH-1 and SCC-1 kleisins leads to the degradation of SMC-1, as judged by the disappearance of SMC-1::GFP fluorescence. Furthermore, COH-1 is the most abundant cohesin kleisin and its cleavage results in the complete disappearance of SMC-1 from most cells, except mitotically active ones.

Mitotic functions of cohesins and condensins

To investigate the mitotic functions of SMC complexes, we induced kleisin cleavage during the L1 stage when 90% of cells are postmitotic[52] and assessed the phenotypic consequences in adults (Fig. 1d and Supplementary Fig. 1e–h). Cleavage of cohesin$^{SCC\text{-}1}$ resulted in developmental delays, morphological changes and a nonfunctional vulva in 64% of the animals (Fig. 1d), further confirming the function of cohesin$^{SCC\text{-}1}$ in mitosis and/or terminal differentiation of the vulva. Simultaneous cleavage of both cohesin$^{SCC\text{-}1}$ and cohesin$^{COH\text{-}1}$ produced phenotypes similar to single cohesin$^{SCC\text{-}1}$ cleavage (Fig. 1d). For condensins, separate cleavage of condensin I/I^{DC} or condensin II slightly delayed late-stage development, yet most animals had no obvious phenotype. Simultaneous cleavage of both condensins resulted in the appearance of phenotypes associated with aberrant vulval development in most animals (Fig. 1d). Condensin I/I^{DC} and II can therefore complement each other's functions, but at least one type of condensin is necessary for faithful postembryonic cell divisions, reminiscent of the subtle changes observed in mammalian cells on individual condensin subunit depletion and the major mitotic defects when both condensins are depleted[53,54].

We further examined seam cell divisions on kleisin cleavage using fluorescent markers[55]. Seam cells divide symmetrically for a subset of them during the second larval stage and asymmetrically once per larval stage, giving rise to a seam cell and a hypodermal cell, which fuses with the rest of the hypoderm[52,56]. The number of seam cells thereby remains constant at each stage, except the second one where it increases from 20 to 32 (Fig. 1e, TEV control animals). Cleavage of cohesin$^{COH\text{-}1}$ or condensin I/I^{DC} did not affect the number of seam cells, whereas cleavage of cohesin$^{SCC\text{-}1}$ or condensin II resulted in decreasing numbers (Fig. 1e). Simultaneous cleavage of both cohesin kleisins had a slight additive effect compared with cohesin$^{SCC\text{-}1}$ cleavage, confirming cohesin$^{SCC\text{-}1}$ as the major mitotic cohesin. Cleavage of both condensins led to a more rapid decrease in seam cell number, reminiscent of the one observed on cleavage of cohesin$^{SCC\text{-}1}$. We conclude that, although quantitatively less abundant, condensin II and cohesin$^{SCC\text{-}1}$ are necessary for postembryonic cellular divisions, whereas condensin I/I^{DC} and cohesin$^{COH\text{-}1}$ are dispensable.

In summary, the data presented above strongly suggest that remaining levels of intact SMC complexes on kleisin cleavage are not able to sustain their function. For both cohesins, one of the two SMC subunits appears degraded on COH-1 and/or SCC-1 cleavage. For condensin I and II, cleaved complexes negatively impact cell divisions. Although the dominant negative effects of cleaved kleisins cannot be ruled out, the observed evidence suggests that SMC complexes lose functionality on kleisin cleavage.

Cleavage of condensin I/I^{DC} reduces lifespan drastically

To assess the physiological effects of cleaving cohesin or condensin kleisins on the whole organism, we assessed the lifespan of animals. Cleaving condensin II or cohesin$^{SCC\text{-}1}$ had minimal impact on lifespan, with animals living nearly as long as TEV control animals (Fig. 1f). By contrast, cleaving condensin I/I^{DC} significantly reduced lifespan, with most animals dying by day 15 and only 3% still alive by day 20, compared with 71% of control animals (Fig. 1f). As no mitotic phenotype was observed in animals after condensin I/I^{DC} cleavage, the lifespan reduction probably stems from the nonmitotic functions of this SMC complex.

Hi-C analysis reveals genome organization at various scales

To characterize genome-folding determinants in nematodes, we conducted high-resolution chromosome conformation capture (Hi-C), in both wild-type and TEV control animals (Fig. 2a,b and Supplementary Figs. 2a and 3). As previously observed[45], autosomes lack the TAD structure found in many multicellular organisms, replaced by large contact domains (Fig. 2a): two multi-megabase domains located on chromosome arms (telomere-proximal domains or T domains) and a large domain located in the chromosome center (C domain). This organization correlates with the spatial segregation of repeat-rich heterochromatic T domains at the nuclear periphery and the transcriptionally more active C domain inside the nuclear lumen (for a review, see ref. 57). Genome-wide Hi-C matrices highlight this long-range organization within and between chromosomes (Fig. 3a–e and Supplementary Fig. 2a). In addition, a crosshatched pattern is observed on a small scale (2–40 kb; Fig. 2a), indicating the presence of smaller compartments embedded into the T and C domains (Fig. 2a and Supplementary Fig. 2a). Principal component analysis (PCA) on the genome-wide observed/expected contact matrix reflected this two-tiered organization (Fig. 2a and Supplementary Fig. 2a): the first eigenvector delineated T/C domains, whereas the second captured the small-scale crosshatch pattern (Fig. 2a and Supplementary Fig. 2a).

Both large domains and small compartments correlated with transcription, yet this correlation was stronger for the latter (Fig. 2c). A comparison with previously characterized chromatin states[58] confirmed this correlation with transcriptional activity (Fig. 2d and Supplementary Fig. 2b,c). T domains were enriched for H3K9-methylated chromatin but retained active chromatin states, because transcriptionally active genes within T domains are interspersed among silent repeats. Conversely, C domains were enriched for active states, yet harbor many Polycomb-marked silent regions (Fig. 2d and Supplementary Fig. 2b). In contrast, small compartments faithfully separated active and silent chromatin (Fig. 2d): small compartments with high second eigenvector values were enriched for active chromatin states, whereas those with low values harbored inactive states (H3K9 and H3K27 methylation). These small compartments are therefore similar to A- and B-type chromatin compartments previously described in mammalian systems[2], although 10× smaller in size. Similar small A- and B-type compartments have been suggested using DNase I Hi-C (ARC-C) and proposed to represent a TAD-like structure[59]. When averaging contact maps on larger A/B compartments (>10 kb), we could indeed highlight insulated domains and the aggregated insulation score between A and B domains showed a minimum at the boundary (Supplementary Fig. 2d,e).

https://doi.org/10.1038/s41588-024-01832-5

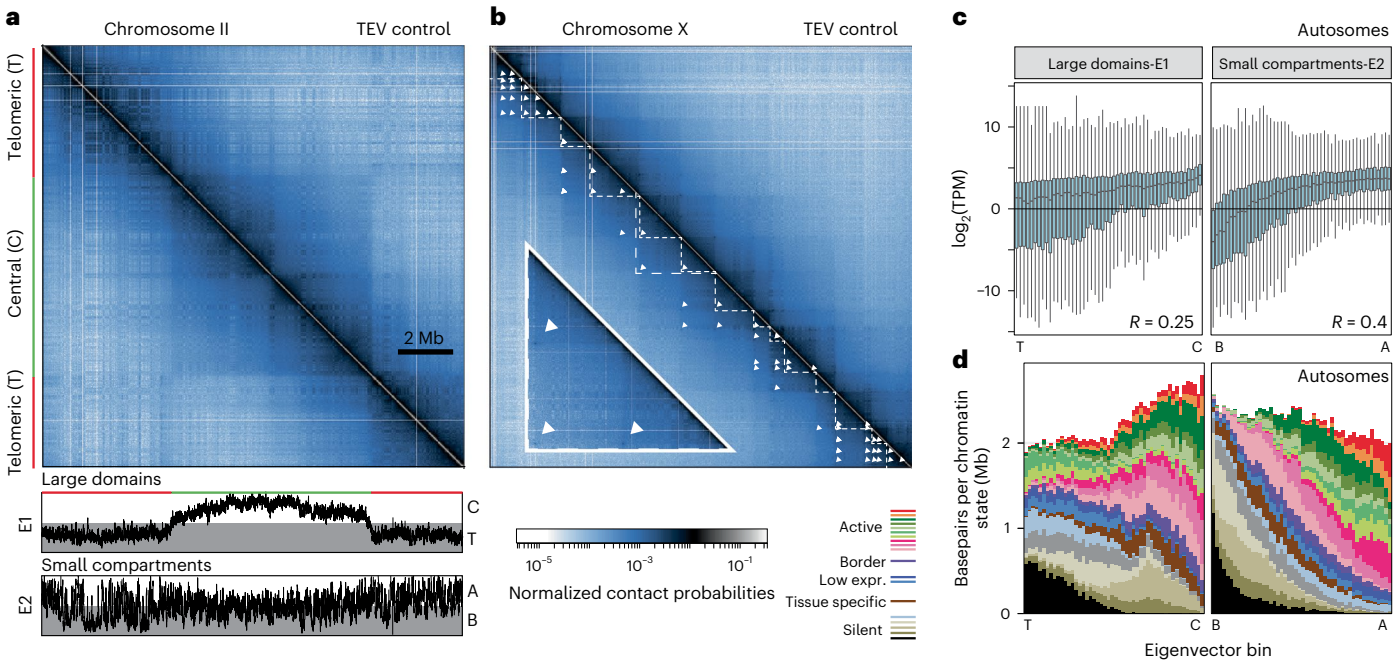

Fig. 2 | *C. elegans* interphase genome is organized at two different scales. **a**, Hi-C contact frequency map for chromosome II in TEV control, L3 stage animals after TEV induction at the L1 stage. The compartment tracks at the bottom show the first and second interchromosomal eigenvectors of the PCA of the genome-wide matrix, with large, megabase-size T/C domains identified in the first one, and small kilobase-size A/B compartments in the second. T/C domains are delineated on the left side of the matrix. **b**, Hi-C contact map of chromosome X in TEV control animals. TADs and loops are highlighted in the lower part of the matrix (dashed lines and white arrowheads, respectively). A blow-up of the central part of the chromosome is shown superimposed on the lower part of the matrix (long dashed lines), highlighting the loops (white arrowheads). For both Hi-C maps, the thin white lines are unmappable genomic regions, for which no Hi-C contacts can be determined using short-read sequencing. **c**, Correlation of first (E1, large domains) and second (E2, smaller compartments) eigenvector values with transcription in TEV control animals. Eigenvector values for 2-kb genomic regions were binned into 50 quantiles. Genomic intervals in bin 1 have therefore the lowest 2% eigenvector values, whereas genomic intervals in bin 50 have the highest ones. For each 2-kb genomic region, the average expression values of the corresponding genomic intervals were determined and grouped into the 50-eigenvector value bins as a boxplot ($n = 756$ regions per eigenvector value bin). The boxplot as in Fig. 1e. Spearman's correlation of $\log_2$(RNA-seq (TPM)) versus eigenvalues for individual 2-kb genomic regions with >0 TPM ($n = 37{,}709$ regions) is shown at the bottom right. **d**, Autosomal chromatin state composition summed over genomic intervals of each eigenvector value bin in **c**, using data from ref. 58. Results for the X chromosome and detailed legend for chromatin states are shown in Supplementary Fig. 2b,c. expr., expression.

In hermaphrodites, the X chromosomes fold into TADs, setting them apart from autosomes (Fig. 2b). TADs require the activity of the X-specific condensin I^{DC} (refs. 31,45,47,60). Although most of the X chromosome lies within a large C domain (see below), small compartments within the TADs form a crosshatched pattern similar to autosomes, which correlates with chromatin states (Supplementary Fig. 2b). High contact probability signals at the corners of the TADs suggest the existence of more stable loops between TAD boundaries (white arrows in Fig. 2b), which have been observed in Hi-ChIP (chromatin immunoprecipitation) experiments with the condensin I^{DC} subunit DPY-27 (ref. 46). These loops span over two or three TAD boundaries.

Condensin I/I^{DC} is the main SMC complex for genome folding

In mammalian cells, cohesin is central to interphase chromosome folding[11–13], via its DNA loop extrusion activity limited by boundary elements bound by CTCF[16,20,21], a transcription factor absent from the nematode genome. To uncover the identity of the SMC complex that drives chromatin looping in nematodes, we performed Hi-C after cleavage of cohesin or condensin kleisins. In contrast to mammalian cells, individual or simultaneous cleavage of cohesin kleisins only slightly decreased contact probabilities at short distances (10–100 kb; Fig. 3a,b,c,f and Supplementary Fig. 2f), demonstrating that cohesins have no significant impact on large-scale interphase chromosome folding. Similarly, condensin II kleisin cleavage did not change Hi-C maps, indicating that its primary function is to ensure proper mitotic chromosome compaction (Fig. 3e,f and Supplementary Fig. 2g). In contrast, cleavage of condensin I/I^{DC} led to significant changes: contact probabilities decreased at distances between 100 kb and 3 Mb and increased at distances >3 Mb (Fig. 3d,f and Supplementary Fig. 2h). Condensin I/I^{DC} therefore promotes long-range contacts between 100 kb and 3 Mb, leading to a decrease of very-long-range contacts.

Condensin I cleavage increases epigenomic compartmentation

By analogy with observations made in mammalian cells on depletion of cohesin, a consequence of condensin I/I^{DC} cleavage should be the reinforcement of A and B compartments[11–13]. Indeed, condensin I/I^{DC} cleavage led to an increase of contact frequency in the crosshatch patterns (Fig. 3g), indicative of the reinforcement of T and C domains within chromosomes, as well as B compartments (Fig. 3d,h). Between autosomes, C domains and B compartments were equally reinforced (Fig. 3h). A and B compartments also saw their size increase by 62% and 54%, respectively (Fig. 3i). Notably, chromosome X showed an increase in interchromosomal contacts with T domains of all autosomes (Fig. 3d), suggesting a relocation of the X chromosome toward the nuclear periphery on condensin I/I^{DC} cleavage, as previously observed[61].

We further analyzed whether alterations in compartments after condensin I/I^{DC} cleavage were associated with specific genomic content of the sequences transitioning compartments (Supplementary Fig. 4). Bins switching toward more B-like compartments were depleted in annotated transposable elements but showed enrichment in noncoding RNAs and transfer RNAs, along with active histone marks. These regions also contained genes exhibiting increased expression after

https://doi.org/10.1038/s41588-024-01832-5

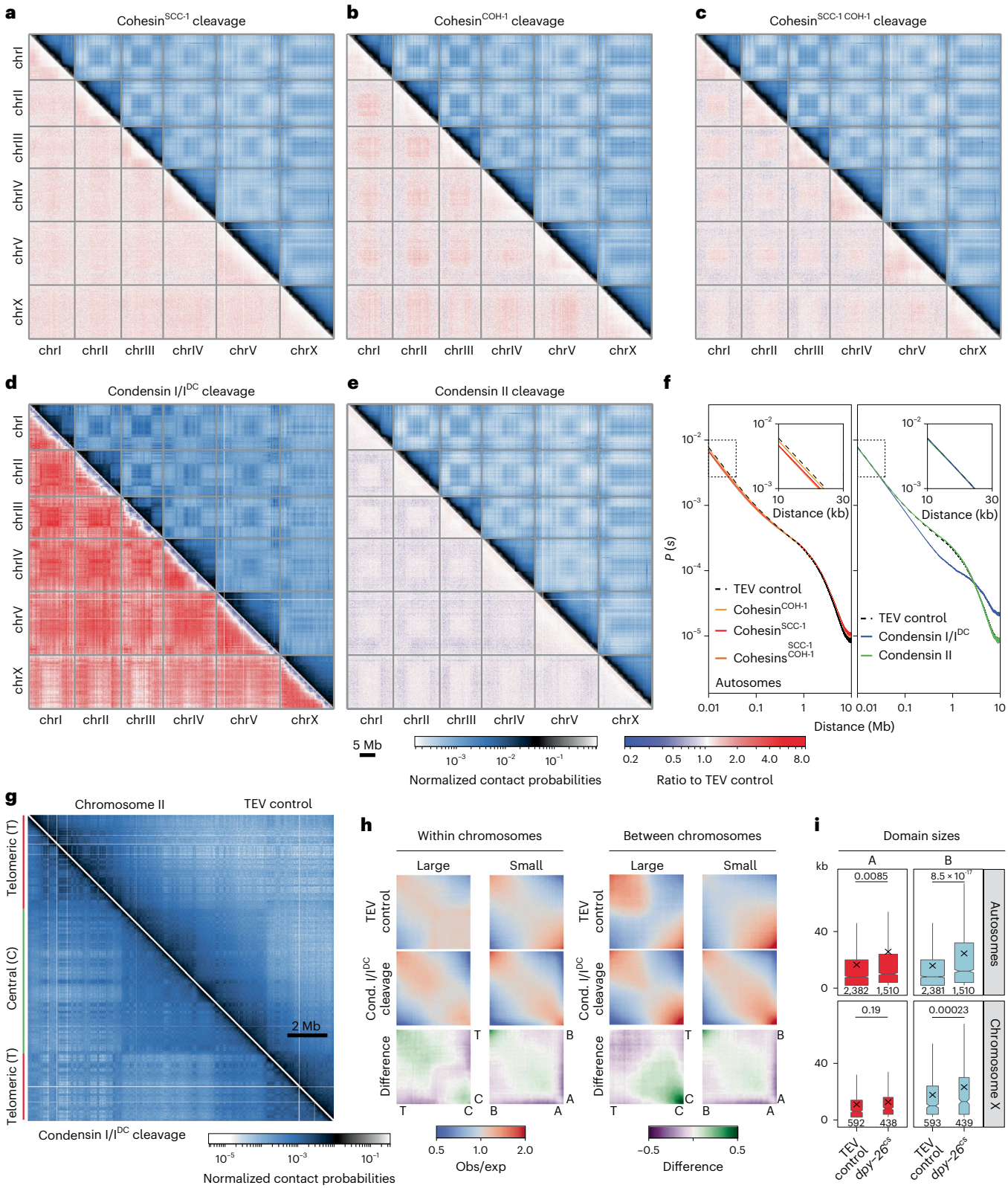

cleavage. Conversely, bins switching toward more A-type compartments did not display such patterns (Supplementary Fig. 4).

Taken together, our analysis demonstrates that condensin I/I^{DC} is the primary SMC complex responsible for chromosome folding in *C. elegans*. Cleavage of condensin I/I^{DC} induces global genome decompaction and an increase in interchromosomal contacts, as well as a significant enhancement of T/C and A/B compartmentalization.

Condensin I/I^{DC} cleavage reveals an X-specific loop compartment

In mammalian cells, loss of cohesin leads to the disappearance of TADs and loops[11–13], structures present only on the X chromosome in *C. elegans*. As for autosomes, cleavage of cohesin and condensin II kleisins had little effect on X-chromosome structure (Supplementary Fig. 2f,g). In contrast, condensin I/I^{DC} cleavage caused major changes

Fig. 3 | Condensin I folds the nematode genome. a–**e**, Genome-wide Hi-C contact maps in L3 animals upon SMC cleavage (upper right) and ratio to TEV control (lower left). TEV protease expression was induced at the L1 stage. The cleaved SMC complexes are indicated on top of the figures: cohesin$^{SCC\text{-}1}$ (**a**); cohesin$^{COH\text{-}1}$ (**b**); cohesin$^{COH\text{-}1}$ and cohesin$^{SCC\text{-}1}$ (**c**); condensin I/IDC (**d**); condensin II (**e**). Pooled data are from two biological replicates per condition. The same color scale was used for all Hi-C maps. **f**, Contact probability decay plots on autosomes for the different cohesin and condensin cleavages. Inset: contact probability decay at short distances (10–30 kb). **g**, Hi-C contact map of chromosome II in TEV control animals (upper right) and on condensin I/I^{DC} cleavage (lower left), highlighting the increased A/B compartmentalization. **h**, Saddle contact probability plots for large T/C domains and small A/B compartments within chromosomes (left) and between chromosomes (right) in TEV control (upper row) and animals after condensin (Cond.) I/I^{DC} cleavage (middle row). The difference between the two conditions is shown in the bottom row. **i**, A and B compartment sizes on autosomes and chromosome X in TEV control and on condensin I/I^{DC} cleavage (*dpy-26*^{cs}). Boxplots are as in Fig. 1e and the 'x's denote the mean domain sizes. The number of compartments in each group and false recovery rate (FDR)-adjusted *P* values from a two-sided Wilcoxon's rank-sum test are shown below and above the boxplots, respectively. chr, chromosome; Obs/exp, observed/expected.

with the disappearance of X-specific TADs (Fig. 4a,b,d). Strikingly, cleavage of condensin I/I^{DC} led to the appearance of dotted lines on the Hi-C map, suggesting the presence of reciprocal loops between 35 individual kilobase-sized regions (Fig. 4a). Manual mapping and automatic detection[62] of the loops showed a high overlap between these regions (hereafter named loop anchors) and TAD boundaries present in control animals (Fig. 4a,b). Although each loop anchor contacted a limited number of neighboring anchors in TEV control animals (Fig. 4c,f), cleavage of condensin I/I^{DC} tripled the number of loops per anchor (Fig. 4c,f), with a threefold increase in the mean size of loops from 1.25 Mb to 3.7 Mb, and the presence of many loops >8 Mb (the X-chromosome size is 17 Mb; Fig. 4f). Average Hi-C contact frequency maps using all combinations of anchors confirmed that contact frequencies between loop anchors increased at small and large distances (Fig. 4e).

MEME motif detection identified the MEX motif in all 35 loop anchors and 34 out of 35 colocalized with previously identified *rex* sites, a subset of MEX motifs with high enrichment for the X-specific condensin I^{DC}-targeting complex (Fig. 4a, bottom, and Supplementary Table 6)[63]. Using a previous classification of *rex* sites[63], 81% of strong *rex* sites (15 out of 17), 50% of intermediate *rex* sites and 29% of weak *rex* sites overlapped with anchors; hence strong *rex* sites are more likely to be loop anchors. Further comparisons with public ChIP-seq demonstrated strong enrichment at loop anchors for condensin I^{DC} and the X-specific-targeting complex subunits SDC-2, SDC-3 and DPY-30 (Fig. 4g). Loop anchors colocalized with a subset of the highest ChIP peaks for these proteins with an average enrichment between 44× and 157× higher than the average enrichment in the surrounding 100-kb regions (Fig. 4g). Surprisingly, other SMC complexes, cohesin$^{SCC\text{-}1}$ and condensin II, showed a similar enrichment at loop anchors, suggesting that these form boundaries for all SMC complexes (Fig. 4g)[64].

Multiple X-chromosome TAD boundaries cluster together

We next asked whether loop anchors form pairs or clusters of more than two anchors. We analyzed Hi-C reads with three or more loci ligated together, accounting for 0.17% of all contacts in both TEV control and condensin I/I^{DC} cleavage libraries (726,736 and 635,546 reads for the X chromosome, respectively). The 3D contact maps at 50-kb resolution were constructed (Fig. 4h)[11,46,65] and average contact maps for all three-way anchor combinations spaced by >500 kb were generated, along with combinations involving a control set of loci (Fig. 4h). Although no significant three-way contacts were observed for control loci, we detected three-way contacts between loop anchors in TEV control libraries, confirming loop anchor clustering[46]. After condensin I/I^{DC} cleavage, the frequency of these three-way contacts between loop anchors more than doubled. This suggests that the X chromosome is folded by anchor hubs to which TADs are attached and these hubs appear to be reinforced in the absence of condensin I/I^{DC}.

The condensin I^{DC}-loading complex forms nuclear bodies

As loop anchors are highly enriched for the SDC complex (Fig. 4g), we asked whether anchor hubs would be detectable in vivo by endogenously tagging SDC-1 or SDC-3. Consistent with previous studies[66–68], both proteins are expressed exclusively in hermaphrodites, show diffuse localization in early embryos and label one or two nuclear territories after dosage compensation onset (data not shown and Fig. 4i,j). Strikingly, fluorescence clustered in individual spots or SDC bodies, with little to no background fluorescence visible outside the clusters (Fig. 4i,j,k). Although linking ChIP, Hi-C and microscopy data is challenging[69], this strongly hints at the presence of loop anchor hubs. Upon condensin I/I^{DC} cleavage, SDC bodies were indistinguishable from TEV control ones (Supplementary Fig. 5), indicating that SDC bodies are independent of condensin I/I^{DC} activity or the presence of TAD. Assuming that these spots represent clustered loop anchors, the absence of modification of the fluorescence pattern indicates that the rosette structure of the X chromosome is present in control animas, yet not visible in Hi-C maps owing to the high number of contacts inside the TADs.

Similar transcriptional impact of cohesin$^{SCC\text{-}1}$ and condensin II cleavage

We next examined the effects of SMC cleavage on gene expression. With the exception of X-linked genes after cleavage of condensin I/I^{DC}, kleisin cleavage had modest effects on gene expression (Supplementary Fig. 6a–c, file S1) with only 3–12% of genes showing different expression levels (154–1,509 genes with $\log_2$(fold-change) (|LFC|) > 0.5;

Fig. 4 | The hermaphrodite X chromosomes form a rosette-like structure. **a**, Hi-C contact frequency matrices in control (upper right) and after cleavage of condensin I/I^{DC} (lower left). The color scale is the same as that in Fig. 2. Left: comparison of regions depicted in the maps highlighting the formation of dashed lines of high contact probabilities on condensin I/I^{DC} cleavage. Loops are depicted as arches on the top and the left side (TEV control, condensin I/I^{DC} cleavage). Bottom: second *cis* eigenvector for condensin I/I^{DC} cleavage for loop anchor detection (local maxima), corresponding loop anchors and *rex* sites[63]. **b**, Insulation scores for the matrices in **a** and the difference between them. **c**, Virtual 4C analysis on three loop anchors in the TEV control and on condensin I/I^{DC} cleavage. **d**, Average observed-over-expected Hi-C contact maps centered on the anchors, highlighting their correlation with TAD boundaries in control conditions and boundary loss on condensin I/I^{DC} cleavage. **e**, Same as **d**, centered on all possible loops between anchors for short-range (<5 Mb) and long-range (>5 Mb) loops, as well as the LFC between the conditions. **f**, Loops per anchor and loop sizes in TEV control and on condensin I/I^{DC} cleavage. The boxplot is as in Fig. 1e, using averaged Hi-C maps from two biological replicates. **g**, ChIP-seq enrichment for the 35 loop anchors detected for DCC subunits (DPY-27 - L3, DPY-30, SDC-2, SDC-3 - embryos), condensin II (KLE-2 - L3) and cohesin (SCC-1 - L3). Data are from refs. 32,59,63,64. **h**, Detection of three-way contacts between loop anchors identified in **a**, using 3D maps built from Hi-C reads with more than two fragments. Average 3D Hi-C maps between all combinations of three loop anchors spaced by at least 500 kb are shown at the bottom, either the middle plane (left) or the sum *z*-projection (right). The number on the upper right corner is the number of identified three-way contacts in the middle voxel/pixel. **i**, Nuclear pattern of SDC-3::mCherry (red) in otherwise wild-type animals. GFP–lamin delineates the nuclear periphery. Scale, 5 µm. **j**, Individual nuclei from the animal in **i**. Scale, 1 µm. **k**, Nuclear pattern of SDC-1::GFP (green). EMR-1::mCherry delineating the nuclear periphery (red). The scale is as in **j**. Imaging experiments were carried out at least twice with similar results.

https://doi.org/10.1038/s41588-024-01832-5

Fig. 5a). Exon–intron split analysis[70] confirmed that most changes occurred at the transcriptional level (Supplementary Fig. 7). Upon cleavage of condensin II, cohesin^{COH-1}, cohesin^{SCC-1} or cohesin$^{COH-1/SCC-1}$, these genes were distributed evenly across all chromosomes, with slightly more genes upregulated than downregulated (Fig. 5a and Supplementary Fig. 6c). Cleavage of both cohesin^{SCC-1} and cohesin^{COH-1} kleisins led to the highest number of misregulated genes. However, there was little overlap between misregulated genes after individual

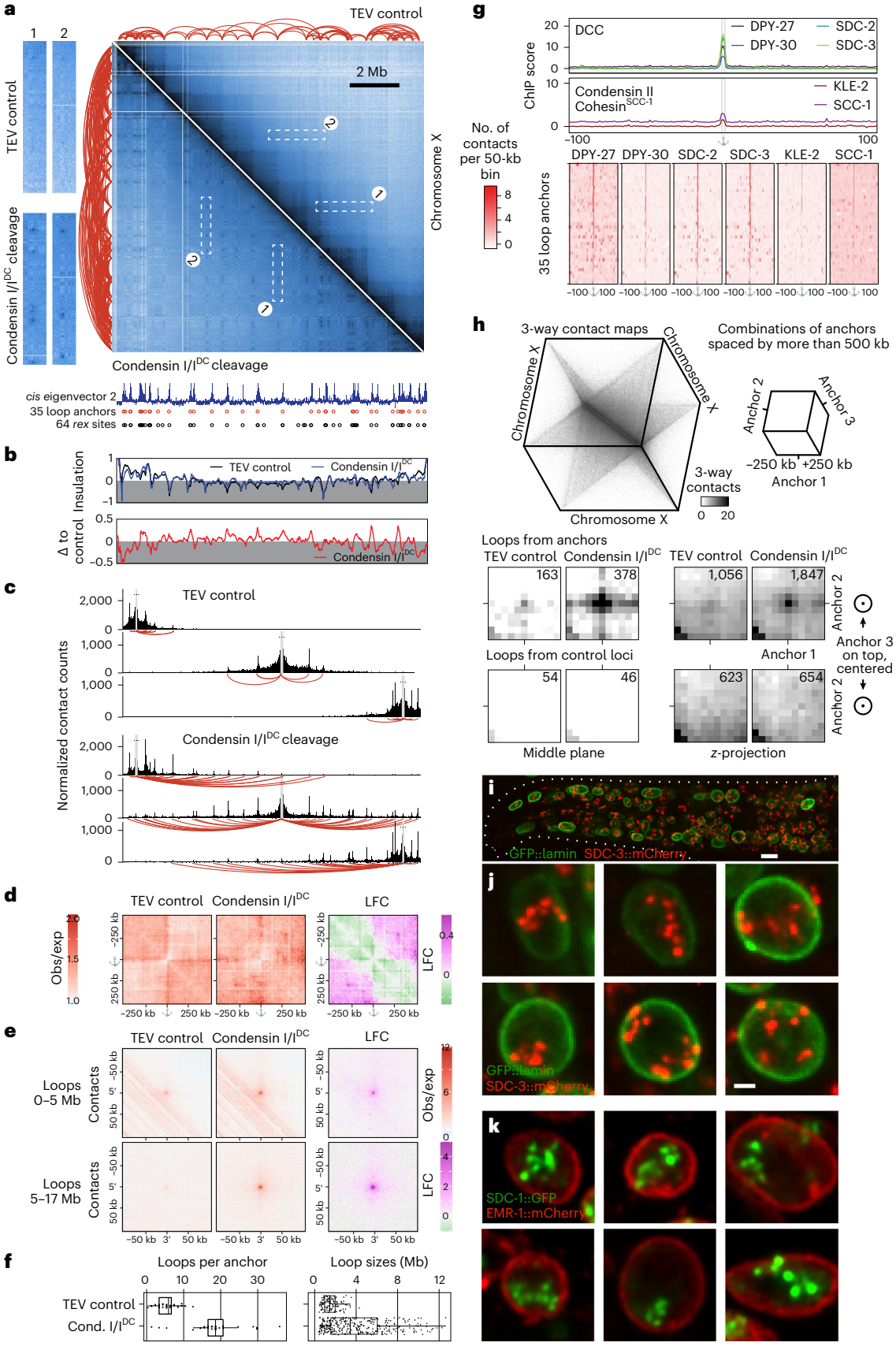

https://doi.org/10.1038/s41588-024-01832-5

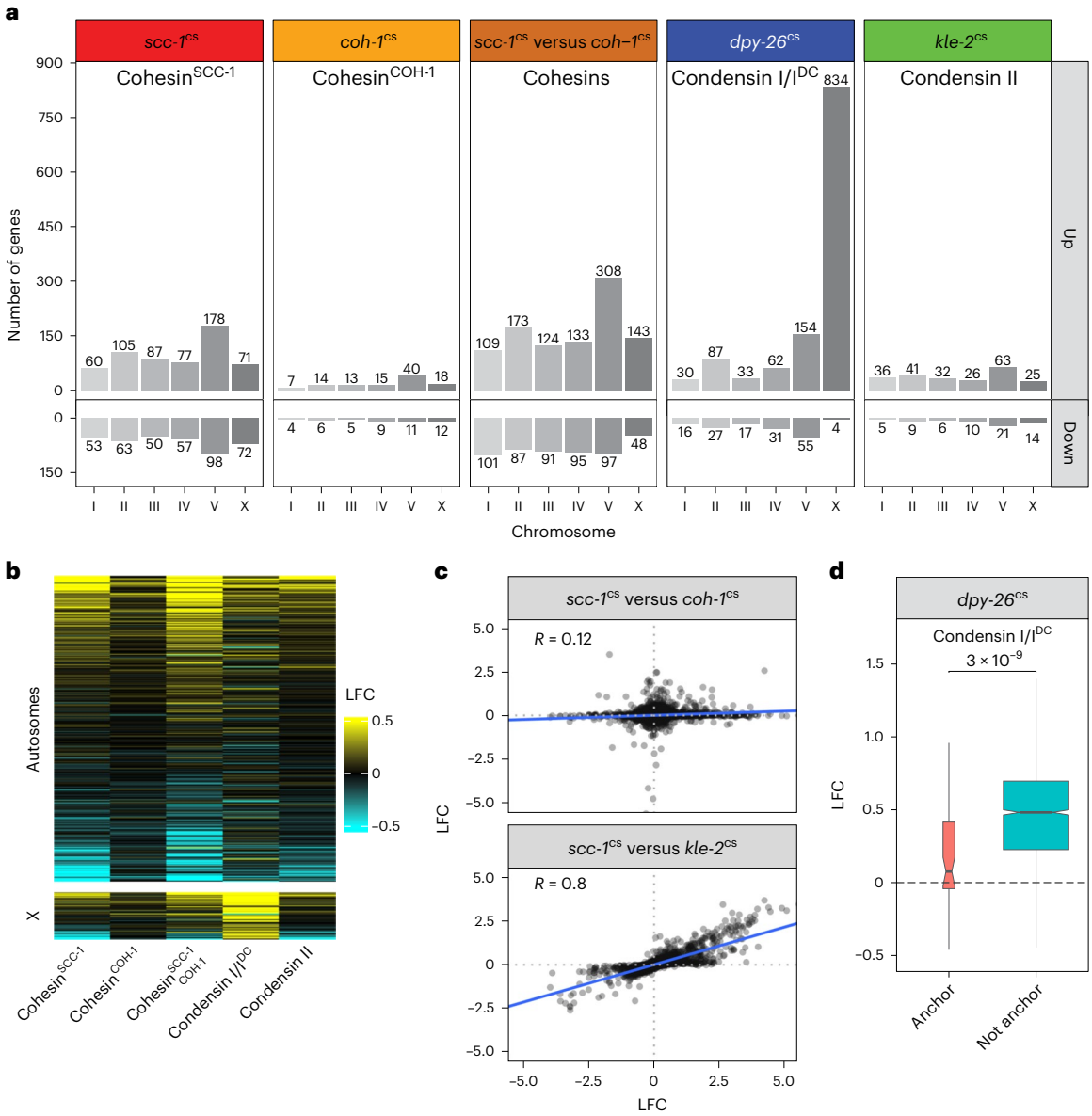

Fig. 5 | Differential gene expression after cleavage of kleisin subunits of different SMC complexes. a, Number of significantly up- and downregulated genes (DESeq2, Wald's test, $P_{adj} < 0.05$, LFC > 0.5) per chromosome on cleavage of the cohesin kleisin subunits *scc-1*^{cs} and *coh-1*^{cs} individually or together, or condensin I/I^{DC} kleisin (*dpy-26*^{cs}) and condensin II kleisin (*kle-2*^{cs}). The number of up-/downregulated genes is shown next to each bar. **b**, Hierarchical clustering of the LFC of 12,465 genes expressed in at least one dataset (DESeq2 independent filtering). Top: 10,792 autosomal genes; bottom: 1,673 X-linked genes. **c**, Correlation of the LFC of 13,734 expressed genes (with at least 10 read counts in total) from the datasets of the two alternative cohesin kleisins (*scc-1*^{cs} and *coh-1*^{cs}, top) and the datasets of condensin II and cohesin^{SCC-1} cleavage (bottom). The blue line indicates the best fit linear regression and Pearson's correlation coefficient is shown. **d**, LFC after cleavage of condensin I/I^{DC} of genes that lie within 10 kb of the 35 loop anchors defined in Fig. 4a ('Anchor', $n = 55$ genes), compared with genes found on the X chromosome that do not overlap with loop anchors ('Not anchor', $n = 1,707$ genes). The FDR-adjusted *P* value from a two-sided Wilcoxon's rank-sum test comparing genes in anchor with nonanchor regions is shown (see Supplementary Fig. 8 for all comparisons). The boxplot shown is the same as that in Fig. 1e.

cleavage of the two cohesin kleisins (Fig. 5b,c and Supplementary Fig. 8a,b), further highlighting the different functions of the two cohesin complexes. In contrast, differentially regulated genes upon cleavage of cohesin^{SCC-1} and condensin II were highly correlated (266 genes overlap; Fig. 5c and Supplementary Fig. 8a,b), with a significant proportion of genes annotated with gene ontology (GO) terms related to proteolysis or stress response (Supplementary File 2). In summary, cleavage of either cohesins or condensin II has relatively minor transcriptional consequences, but a common set of genes appears to be regulated by cohesin^{SCC-1} and condensin II, possibly as a result of their common mitotic function.

Cleavage of condensin I/I^{DC} alleviates dosage compensation

The cleavage of condensin I/I^{DC} led to the most significant changes in gene expression on chromosome X. Half of the expressed X-linked genes showed significantly higher expression (834 out of 1,604), whereas only 4 were downregulated (Fig. 5a,b and Supplementary Fig. 6b,c). The main effect of condensin I/I^{DC} cleavage on gene expression is, thereby, the relief of X-linked repression, owing to the cleavage of condensin I^{DC} (ref. 44). Upregulated genes overlapped significantly with X-linked genes upregulated after *dpy-27* knock-down[32] or mutation of the dosage compensation complex (DCC)-associated *dpy-21* H4K20 demethylase gene[31] (25% and 46%). In contrast to mammalian cells on cohesin depletion[12],

there was no evidence for pervasive upregulation of noncoding RNAs or for general misregulation of transposons or repetitive sequences (data not shown). It is interesting that X-linked gene upregulation, in close vicinity to the loop anchors identified above, bound by the SDC complex, was significantly lower on condensin I/I^{DC} cleavage than on the rest of the chromosome (Fig. 5d and Supplementary Fig. 8c). In nonanchor regions, 48% of genes (823 of 1707) were significantly upregulated, whereas. in 10-kb regions around loop anchors, only 11% were upregulated (6 of 55). Gene regulation is thereby largely maintained close to sites bound by the SDC subunits of the DCC but not inside the TADs delimited by these loop anchors.

Impaired dosage compensation leads to reduced lifespan

Our findings uncovered two consequences of condensin I/I^{DC} cleavage: a widespread loss of chromosome compaction on all chromosomes and transcriptional upregulation of X-linked genes as a result of the loss of dosage compensation, both potentially contributing to the observed decrease in lifespan (Fig. 1f). To differentiate between these possibilities, we assessed the lifespan of animals after the loss of dosage compensation induced by auxin degron-mediated degradation of SDC-3, a crucial factor for condensin I^{DC} enrichment on the X chromosome[66] (Supplementary Fig. 9a). SDC-3 degradation resulted in a decline of the TAD structure of the X chromosomes (Supplementary Fig. 9b–e) and an elevation of X-linked gene expression, albeit to a lesser degree than condensin I/I^{DC} cleavage (Supplementary Fig. 9f,g). On control media lacking auxin, animals exhibited a lifespan comparable to that of TEV control animals (Fig. 1g, black lines), the slightly longer lifespan attributed to heat shock previously shown to increase lifespan[71](to induce TEV expression). Conversely, animals grown on auxin displayed a lifespan akin to that observed after cleavage of condensin I/I^{DC} (Fig. 1g, blue lines). In addition, male animals, which do not require dosage compensation, exhibited a minor increase in healthspan after condensin I cleavage (Fig. 1h). Therefore, the reduction in lifespan subsequent to condensin I/I^{DC} cleavage is not attributable to widespread chromosome unfolding but rather to X-specific disruption of chromosome structure and the consequent upregulation of X-linked genes.

Discussion

Holocentric genomes are widely distributed in nature[72], yet their interphase folding mechanisms remain elusive. In the present study, we unveil that in *C. elegans*, genome organization is controlled by both epigenomic compartmentalization and condensin I/I^{DC} activity. At a multi-megabase scale, chromosomes segregate into arms and central regions with arms forming perinuclear domains rich in repeats and H3K9-methylated heterochromatin[73–77]. Meanwhile, more transcriptionally active central regions reside in the nuclear lumen. At a finer 2- to 100-kb scale, regions with similar epigenomic states preferentially contact each other, forming small A and B compartments, 10–100× smaller than those observed in mammalian and *Drosophila* genomes[2,78]. Unlike mammals, in which chromatin looping and megabase-scale TAD formation occur through the loop extrusion activity of cohesin coupled with oriented boundary elements, large-scale chromosome folding in *C. elegans* is primarily mediated by condensin I/I^{DC}. Cleaving this complex leads to global decompaction, increased interchromosomal contacts and enhanced T/C and A/B compartmentalization. Similar long-range (>100 kb) looping activity of condensin is observed in budding and fission yeast[23,27] where condensin mutations also increase chromosomal mixing, although whether this effect is direct remains unclear[27,79].

Why does condensin I assume the function of cohesin? One possible reason could be the holocentric nature of nematode chromosomes. In mammals, most cohesins are removed from chromosome arms before anaphase, whereas complexes at the centromeres ensure the cohesion of sister chromatids[22]. However, holocentric chromosomes complicate the distinction between centromeric and noncentromeric cohesin populations, because nematode centromeres are defined by the binding of transcription factors and active transcription[80]. By repurposing condensin I/I^{DC} as an interphase, long-range loop extruder and duplicating cohesins with one variant dedicated solely to mitotic functions, it would be possible to functionally separate SMC complexes involved in sister chromatid cohesion from those involved in interphasic genome looping[34].

It is interesting that nematodes lack a CTCF homolog or any well-defined boundary elements involved in TAD formation in mammals or *Drosophila* spp. This suggests that genome folding primarily relies on T/C domains and A/B compartments, rather than TADs[78,81]. The lack of TADs on autosomes also implies that transcriptional regulation is performed by proximal enhancers situated near their target promoters, because the activity of enhancers cannot be constrained by TADs as in mammals[10]. In fact, all characterized enhancer sequences are located within 5 kb of their presumed target gene[82,83], in contrast to gene regulation in mammals where enhancers can be located megabases away from their target gene and the TAD structure[10] limits their activity.

In mammals, multiple studies have shown that lack of cohesins has little transcriptional effect on gene expression under stable conditions[11,12]. Cleavage of the major *C. elegans* long-range loop extruder, condensin I, has equally little effect on autosomal gene expression (Fig. 5a). Recent studies in budding and fission yeast have similarly shown that condensin depletion or cleavage has little effect on transcription[23,84], and these effects are probably indirect due to chromosome missegregation. Condensin has, however, been implicated in gene downregulation in response to environmental stimuli such as starvation or quiescence[85,86]. With regard to animals, it is less clear whether condensins play a role in gene regulation. In *Drosophila* spp., early reports suggest that the condensin I kleisin is necessary for *Fab-7* Polycomb responsive element repression[87]. More recently, the CAP-G subunit of condensin I was shown to be important for proper neuronal gene expression, yet genes were equally up- and downregulated and the involvement of the condensin I holocomplex remains unclear[88]. In our study, condensin II cleavage led to only a few misregulated genes without any chromosome specificity, with more genes being up- than downregulated, similar to condensin I/I^{DC} cleavage (Fig. 5a). These misregulated genes might result from an indirect effect of failed mitosis because they correlate strongly with genes misregulated on cleavage of the cohesin^{SCC-1} complex solely expressed in dividing cells[34] (Fig. 5c). Several studies have shown a role for condensin II in gene regulation in other experimental systems, yet it is unclear whether the complex is involved in repression or activation. In *Drosophila* spp., the whole complex is involved in transvection by repressing gene expression in *trans*[89] whereas the CAP-D3 subunit is necessary for activation of antimicrobial peptide expression[90]. Similarly, the murine CAP-G2 condensin II component is essential for erythroid cell differentiation and appears to repress gene expression[91], but whether this is mediated by the condensin II holocomplex remains unclear.

In hermaphrodite nematodes, TADs are uniquely present on X chromosomes as a result of the SDC-mediated loading of the X-specific variant of condensin I, condensin I^{DC} (refs. 45,47) and cleavage of condensin I/I^{DC} results in the loss of all TADs. As TAD formation requires dynamic loop extrusion limited by boundaries[20], and condensins are indeed DNA loop extruders[15,17], our findings, together with recent results showing that the ATPase activity of DPY-27 is necessary for its binding to the X chromosome[92], strongly suggest a model in which the SDC complex recruits condensin I^{DC} to *rex* sites and both initiates and limits loop extrusion, leading to the formation of TADs. The function of X-chromosome TADs in nematodes appears to be quite different from mammalian TADs, which limit the search space of enhancers[5,10]. Indeed, no ectopic expression of the X-linked gene *unc-3* was observed on condensin I/I^{DC} cleavage (data not shown), thus reinforcing the idea that genes are controlled by enhancers locally (within kilobases of their target genes).

Surprisingly, the cleavage of condensin I/I^{DC} strengthens a loop compartment formed by reciprocal contacts between 35 loci highly enriched for the SDC complex[64], colocalizing with *rex* sites[93] and TAD boundaries[47]. This reinforcement of loops between TAD boundaries mirrors observations in mammalian cells where cohesin stabilization by WAPL knock-down or cohesin^{STAG1} acetylation[94,95] leads to long-range loop extrusion. However, long-range loop extrusion is unlikely to cause the reinforcement of the loop compartment, because our experiments imply release of condensin I/I^{DC} from chromatin, rather than stabilization of loop extruders. Two studies in mammals have reported the appearance of a loop compartment on cohesin depletion as visualized by aligned dots on Hi-C maps[11,96]. In these studies, loop anchors are either strongly clustered enhancers bound by the transcriptional co-activators BRD4 and MED1 (ref. 97) or regions bound by PRC1 complexes[96], both of which are known to form condensates[97–99]. In nematodes, genomic segments in the loop compartment are bound by the SDC proteins and tagging of SDC proteins led us to discover SDC bodies, previously unseen nuclear clusters that could potentially be condensates. At the transcriptional level, cleavage of condensin I^{DC} cleavage leads to the upregulation of most X-linked genes, underscoring the importance of the continuous presence of condensin I/I^{DC} on X chromatin for maintenance of X-linked gene regulation. Strikingly, after condensin I/I^{DC} cleavage, dosage compensation is maintained near loop anchors, probably included in SDC bodies. Further experiments should investigate whether SDC bodies are indeed condensates and whether looping chromatin through condensates via condensin I/I^{DC} regulates gene expression. From a physiological perspective, the imbalance in gene expression created by condensin I/I^{DC} cleavage between X chromosomes and autosomes significantly shortens the animal's lifespan, whereas autosomal decompaction does not lead to any major phenotypes.

In conclusion, our study presents evidence supporting the functional substitution of cohesin by condensin I in holocentric nematodes for interphase genome folding, together with the identification of nuclear bodies involved in X-linked gene downregulation by condensin I^{DC}. Further characterization in other holocentric species will help determine whether the use of condensin I is unique to *C. elegans* or convergent evolution has led to similar mechanisms in other holocentric organisms[100].

Online content

Any methods, additional references, Nature Portfolio reporting summaries, source data, extended data, supplementary information, acknowledgements, peer review information; details of author contributions and competing interests; and statements of data and code availability are available at https://doi.org/10.1038/s41588-024-01832-5.

References

1. Dekker, J., Rippe, K., Dekker, M. & Kleckner, N. Capturing chromosome conformation. *Science* **295**, 1306–1311 (2002).
2. Lieberman-Aiden, E. et al. Comprehensive mapping of long-range interactions reveals folding principles of the human genome. *Science* **326**, 289–293 (2009).
3. Cattoni, D. I. et al. Single-cell absolute contact probability detection reveals chromosomes are organized by multiple low-frequency yet specific interactions. *Nat. Commun.* **8**, 1753 (2017).
4. Stevens, T. J. et al. 3D structures of individual mammalian genomes studied by single-cell Hi-C. *Nature* **544**, 59–64 (2017).
5. Lupianez, D. G. et al. Disruptions of topological chromatin domains cause pathogenic rewiring of gene-enhancer interactions. *Cell* **161**, 1012–1025 (2015).
6. Hnisz, D. et al. Activation of proto-oncogenes by disruption of chromosome neighborhoods. *Science* **351**, 1454–1458 (2016).
7. Flavahan, W. A. et al. Insulator dysfunction and oncogene activation in IDH mutant gliomas. *Nature* **529**, 110–114 (2016).
8. Nora, E. P. et al. Spatial partitioning of the regulatory landscape of the X-inactivation centre. *Nature* **485**, 381–385 (2012).
9. Dixon, J. R. et al. Chromatin architecture reorganization during stem cell differentiation. *Nature* **518**, 331–336 (2015).
10. Zuin, J. et al. Nonlinear control of transcription through enhancer–promoter interactions. *Nature* **604**, 571–577 (2022).
11. Rao, S. S. P. et al. Cohesin loss eliminates all loop domains. *Cell* **171**, 305–320.e24 (2017).
12. Schwarzer, W. et al. Two independent modes of chromatin organization revealed by cohesin removal. *Nature* **551**, 51–56 (2017).
13. Wutz, G. et al. Topologically associating domains and chromatin loops depend on cohesin and are regulated by CTCF, WAPL, and PDS5 proteins. *EMBO J.* **36**, 3573–3599 (2017).
14. Rosin, L. F., Nguyen, S. C. & Joyce, E. F. Condensin II drives large-scale folding and spatial partitioning of interphase chromosomes in *Drosophila* nuclei. *PLoS Genet.* **14**, e1007393 (2018).
15. Ganji, M. et al. Real-time imaging of DNA loop extrusion by condensin. *Science* **360**, 102–105 (2018).
16. Davidson, I. F. et al. DNA loop extrusion by human cohesin. *Science* **366**, 1338–1345 (2019).
17. Kong, M. et al. Human condensin I and II drive extensive ATP-dependent compaction of nucleosome-bound DNA. *Mol. Cell* **79**, 99–114.e9 (2020).
18. Golfier, S., Quail, T., Kimura, H. & Brugués, J. Cohesin and condensin extrude DNA loops in a cell cycle-dependent manner. *eLife* **9**, e53885 (2020).
19. Sanborn, A. L. et al. Chromatin extrusion explains key features of loop and domain formation in wild-type and engineered genomes. *Proc. Natl Acad. Sci. USA* **112**, E6456–E6465 (2015).
20. Fudenberg, G. et al. Formation of chromosomal domains by loop extrusion. *Cell Rep.* **15**, 2038–2049 (2016).
21. Li, Y. et al. The structural basis for cohesin–CTCF-anchored loops. *Nature* **578**, 472–476 (2020).
22. Yatskevich, S., Rhodes, J. & Nasmyth, K. Organization of chromosomal DNA by SMC complexes. *Annu. Rev. Genet.* **53**, 445–482 (2019).
23. Paul, M. R., Markowitz, T. E., Hochwagen, A. & Ercan, S. Condensin depletion causes genome decompaction without altering the level of global gene expression in *Saccharomyces cerevisiae*. *Genetics* **210**, 331–344 (2018).
24. Schalbetter, S. A. et al. SMC complexes differentially compact mitotic chromosomes according to genomic context. *Nat. Cell Biol.* **19**, 1071–1080 (2017).
25. Kim, K.-D., Tanizawa, H., Iwasaki, O. & Noma, K.-I. Transcription factors mediate condensin recruitment and global chromosomal organization in fission yeast. *Nat. Genet.* **48**, 1242–1252 (2016).
26. Tanizawa, H., Kim, K.-D., Iwasaki, O. & Noma, K.-I. Architectural alterations of the fission yeast genome during the cell cycle. *Nat. Struct. Mol. Biol.* **24**, 965–976 (2017).
27. Kakui, Y. et al. Fission yeast condensin contributes to interphase chromatin organization and prevents transcription-coupled DNA damage. *Genome Biol.* **21**, 272 (2020).
28. Hoencamp, C. et al. 3D genomics across the tree of life reveals condensin II as a determinant of architecture type. *Science* **372**, 984–989 (2021).
29. Walther, N. et al. A quantitative map of human condensins provides new insights into mitotic chromosome architecture. *J. Cell Biol.* **217**, 2309–2328 (2018).
30. Abdennur, N., Schwarzer, W., Pekowska, A. & Shaltiel, I. A. Condensin II inactivation in interphase does not affect chromatin folding or gene expression. Preprint at *BioRxiv* https://doi.org/10.1101/437459 (2018).

31. Brejc, K. et al. Dynamic control of X chromosome conformation and repression by a histone H4K20 demethylase. *Cell* **171**, 85–102.e23 (2017).
32. Kramer, M. et al. Developmental dynamics of X-chromosome dosage compensation by the DCC and H4K20me1 in *C. elegans*. *PLoS Genet.* **11**, e1005698 (2015).
33. Csankovszki, G. et al. Three distinct condensin complexes control *C. elegans* chromosome dynamics. *Curr. Biol.* **19**, 9–19 (2009).
34. Mito, Y., Sugimoto, A. & Yamamoto, M. Distinct developmental function of two *Caenorhabditis elegans* homologs of the cohesin subunit Scc1/Rad21. *Mol. Biol. Cell* **14**, 2399–2409 (2003).
35. Haering, C. H. & Gruber, S. SnapShot: SMC protein complexes part I. *Cell* **164**, 326–326.e1 (2016).
36. Seitan, V. C. et al. Metazoan Scc4 homologs link sister chromatid cohesion to cell and axon migration guidance. *PLoS Biol.* **4**, e242 (2006).
37. Wang, F., Yoder, J., Antoshechkin, I. & Han, M. *Caenorhabditis elegans* EVL-14/PDS-5 and SCC-3 are essential for sister chromatid cohesion in meiosis and mitosis. *Mol. Cell. Biol.* **23**, 7698–7707 (2003).
38. Chan, R. C. et al. Chromosome cohesion is regulated by a clock gene paralogue TIM-1. *Nature* **423**, 1002–1009 (2003).
39. Ma, H. et al. A highly efficient multifunctional tandem affinity purification approach applicable to diverse organisms. *Mol. Cell. Proteom.* **11**, 501–511 (2012).
40. Maddox, P. S., Portier, N., Desai, A. & Oegema, K. Molecular analysis of mitotic chromosome condensation using a quantitative time-resolved fluorescence microscopy assay. *Proc. Natl Acad. Sci. USA* **103**, 15097–15102 (2006).
41. Hagstrom, K. A., Holmes, V. F., Cozzarelli, N. R. & Meyer, B. J. *C. elegans* condensin promotes mitotic chromosome architecture, centromere organization, and sister chromatid segregation during mitosis and meiosis. *Genes Dev.* **16**, 729–742 (2002).
42. Stear, J. H. & Roth, M. B. Characterization of HCP-6, a *C. elegans* protein required to prevent chromosome twisting and merotelic attachment. *Genes Dev.* **16**, 1498–1508 (2002).
43. Pasierbek, P. et al. The *Caenorhabditis elegans* SCC-3 homologue is required for meiotic synapsis and for proper chromosome disjunction in mitosis and meiosis. *Exp. Cell. Res.* **289**, 245–255 (2003).
44. Meyer, B. J. Mechanisms of sex determination and X-chromosome dosage compensation. *Genetics* **220**, iyab197 (2022).
45. Crane, E. et al. Condensin-driven remodelling of X chromosome topology during dosage compensation. *Nature* **523**, 240–244 (2015).
46. Rowley, M. J. et al. Analysis of Hi-C data using SIP effectively identifies loops in organisms from *C. elegans* to mammals. *Genome Res.* **30**, 447–458 (2020).
47. Kim, J. et al. Condensin DC loads and spreads from recruitment sites to create loop-anchored TADs in *C. elegans*. *eLife* **11**, e68745 (2022).
48. Pauli, A. et al. Cell-type-specific TEV protease cleavage reveals cohesin functions in *Drosoophila* neurons. *Dev. Cell* **14**, 239–251 (2008).
49. Nguyen, H. Q. et al. *Drosophila* casein kinase I alpha regulates homolog pairing and genome organization by modulating condensin II subunit Cap-H2 levels. *PLoS Genet.* **11**, e1005014 (2015).
50. Buster, D. W. et al. SCFSlimb ubiquitin ligase suppresses condensin II–mediated nuclear reorganization by degrading Cap-H2. *J. Cell Biol.* **201**, 49–63 (2013).
51. Crawley, O. et al. Cohesin-interacting protein WAPL-1 regulates meiotic chromosome structure and cohesion by antagonizing specific cohesin complexes. *eLife* **5**, e10851 (2016).
52. Sulston, J. E. & Horvitz, H. R. Post-embryonic cell lineages of the nematode, *Caenorhabditis elegans*. *Dev. Biol.* **56**, 110–156 (1977).
53. Hirota, T., Gerlich, D., Koch, B., Ellenberg, J. & Peters, J.-M. Distinct functions of condensin I and II in mitotic chromosome assembly. *J. Cell Sci.* **117**, 6435–6445 (2004).
54. Gerlich, D., Hirota, T., Koch, B., Peters, J.-M. & Ellenberg, J. Condensin I stabilizes chromosomes mechanically through a dynamic interaction in live cells. *Curr. Biol.* **16**, 333–344 (2006).
55. Koh, K. & Rothman, J. H. ELT-5 and ELT-6 are required continuously to regulate epidermal seam cell differentiation and cell fusion in *C. elegans*. *Development* **128**, 2867–2880 (2001).
56. Singh, R. N. & Sulston, J. E. Some observations on moulting in *Caenorhabditis elegans*. *Nematologica* **24**, 63–71 (1978).
57. Sharma, R. & Meister, P. Nuclear organization in the nematode *C. elegans*. *Curr. Opin. Cell Biol.* **25**, 395–402 (2013).
58. Evans, K. J. et al. Stable *Caenorhabditis elegans* chromatin domains separate broadly expressed and developmentally regulated genes. *Proc. Natl Acad. Sci. USA* **113**, E7020–E7029 (2016).
59. Huang, N. et al. Accessible Region Conformation Capture (ARC-C) gives high-resolution insights into genome architecture and regulation. *Genome Res.* **32**, 357–366 (2022).
60. Anderson, E. C. et al. X chromosome domain architecture regulates *Caenorhabditis elegans* lifespan but not dosage compensation. *Dev. Cell* **51**, 192–207.e6 (2019).
61. Sharma, R. et al. Differential spatial and structural organization of the X chromosome underlies dosage compensation in *C. elegans*. *Genes Dev.* **28**, 2591–2596 (2014).
62. Roayaei Ardakany, A., Gezer, H. T., Lonardi, S. & Ay, F. Mustache: multi-scale detection of chromatin loops from Hi-C and Micro-C maps using scale-space representation. *Genome Biol.* **21**, 256 (2020).
63. Albritton, S. E., Kranz, A.-L., Winterkorn, L. H., Street, L. A. & Ercan, S. Cooperation between a hierarchical set of recruitment sites targets the X chromosome for dosage compensation. *eLife* **6**, e23645 (2017).
64. Kranz, A. L. et al. Genome-wide analysis of condensin binding in *Caenorhabditis elegans*. *Genome Biol.* **14**, R112 (2013).
65. Allahyar, A. et al. Enhancer hubs and loop collisions identified from single-allele topologies. *Nat. Genet.* **50**, 1151–1160 (2018).
66. Davis, T. L. & Meyer, B. J. SDC-3 coordinates the assembly of a dosage compensation complex on the nematode X chromosome. *Development* **124**, 1019–1031 (1997).
67. Yonker, S. A. & Meyer, B. J. Recruitment of *C. elegans* dosage compensation proteins for gene-specific versus chromosome-wide repression. *Development* **130**, 6519–6532 (2003).
68. Ercan, S. et al. X chromosome repression by localization of the *C. elegans* dosage compensation machinery to sites of transcription initiation. *Nat. Genet.* **39**, 403–408 (2007).
69. Fudenberg, G. & Imakaev, M. FISH-ing for captured contacts: towards reconciling FISH and 3C. *Nat. Methods* **14**, 673–678 (2017).
70. Gaidatzis, D., Burger, L., Florescu, M. & Stadler, M. B. Analysis of intronic and exonic reads in RNA-seq data characterizes transcriptional and post-transcriptional regulation. *Nat. Biotechnol.* **33**, 722–729 (2015).
71. Lithgow, G. J., White, T. M., Melov, S. & Johnson, T. E. Thermotolerance and extended life-span conferred by single-gene mutations and induced by thermal stress. *Proc. Natl Acad. Sci. USA* **92**, 7540–7544 (1995).
72. Mandrioli, M. & Manicardi, G. C. Holocentric chromosomes. *PLoS Genet.* **16**, e1008918 (2020).
73. Towbin, B. D. et al. Step-wise methylation of histone H3K9 positions heterochromatin at the nuclear periphery. *Cell* **150**, 934–947 (2012).
74. Liu, T. et al. Broad chromosomal domains of histone modification patterns in *C. elegans*. *Genome Res.* **21**, 227–236 (2011).

75. Ikegami, K., Egelhofer, T. A., Strome, S. & Lieb, J. D. *Caenorhabditis elegans* chromosome arms are anchored to the nuclear membrane via discontinuous association with LEM-2. *Genome Biol.* **11**, R120 (2010).
76. Gonzalez-Aguilera, C. et al. Genome-wide analysis links emerin to neuromuscular junction activity in *Caenorhabditis elegans*. *Genome Biol.* **15**, R21 (2014).
77. Bian, Q., Anderson, E. C., Yang, Q. & Meyer, B. J. Histone H3K9 methylation promotes formation of genome compartments in *Caenorhabditis elegans* via chromosome compaction and perinuclear anchoring. *Proc. Natl Acad. Sci. USA* **117**, 11459–11470 (2020).
78. Sexton, T. et al. Three-dimensional folding and functional organization principles of the *Drosophila* genome. *Cell* **148**, 458–472 (2012).
79. Iwasaki, O., Corcoran, C. J. & Noma, K.-I. Involvement of condensin-directed gene associations in the organization and regulation of chromosome territories during the cell cycle. *Nucleic Acids Res.* **44**, 3618–3628 (2016).
80. Steiner, F. A. & Henikoff, S. Holocentromeres are dispersed point centromeres localized at transcription factor hotspots. *eLife* **3**, e02025 (2014).
81. Dixon, J. R. et al. Topological domains in mammalian genomes identified by analysis of chromatin interactions. *Nature* **485**, 376–380 (2012).
82. Jänes, J. et al. Chromatin accessibility dynamics across *C. elegans* development and ageing. *eLife* **7**, e37344 (2018).
83. Daugherty, A. C. et al. Chromatin accessibility dynamics reveal novel functional enhancers in *C. elegans*. *Genome Res.* **27**, 2096–2107 (2017).
84. Hocquet, C. et al. Condensin controls cellular RNA levels through the accurate segregation of chromosomes instead of directly regulating transcription. *eLife* **7**, e38517 (2018).
85. Lancaster, L., Patel, H., Kelly, G. & Uhlmann, F. A role for condensin in mediating transcriptional adaptation to environmental stimuli. *Life Sci. Alliance* **4**, e202000961 (2021).
86. Swygert, S. G. et al. Condensin-dependent chromatin compaction represses transcription globally during quiescence. *Mol. Cell* **73**, 533–546.e4 (2019).
87. Lupo, R., Breiling, A., Bianchi, M. E. & Orlando, V. *Drosophila* chromosome condensation proteins topoisomerase II and Barren colocalize with Polycomb and maintain *Fab-7* PRE silencing. *Mol. Cell* **7**, 127–136 (2001).
88. Hassan, A. et al. Condensin I subunit Cap-G is essential for proper gene expression during the maturation of post-mitotic neurons. *eLife* **9**, e55159 (2020).
89. Hartl, T. A., Smith, H. F. & Bosco, G. Chromosome alignment and transvection are antagonized by condensin II. *Science* **322**, 1384–1387 (2008).
90. Longworth, M. S. et al. A shared role for RBF1 and dCAP-D3 in the regulation of transcription with consequences for innate immunity. *PLoS Genet.* **8**, e1002618 (2012).
91. Xu, Y., Leung, C. G., Lee, D. C., Kennedy, B. K. & Crispino, J. D. MTB, the murine homolog of condensin II subunit CAP-G2, represses transcription and promotes erythroid cell differentiation. *Leukemia* **20**, 1261–1269 (2006).
92. Breimann, L. et al. The histone H4 lysine 20 demethylase DPY-21 regulates the dynamics of condensin DC binding. *J. Cell Sci.* **135**, jcs258818 (2022).
93. Albritton, S. E. & Ercan, S. *Caenorhabditis elegans* dosage compensation: insights into condensin-mediated gene regulation. *Trends Genet.* **34**, 41–53 (2018).
94. Wutz, G. et al. ESCO1 and CTCF enable formation of long chromatin loops by protecting cohesinSTAG1 from WAPL. *eLife* **9**, e52091 (2020).
95. Haarhuis, J. H. I. et al. The cohesin release factor WAPL restricts chromatin loop extension. *Cell* **169**, 693–707.e14 (2017).
96. Rhodes, J. D. P. et al. Cohesin disrupts polycomb-dependent chromosome interactions in embryonic stem cells. *Cell Rep.* **30**, 820–835.e10 (2020).
97. Sabari, B. R. et al. Coactivator condensation at super-enhancers links phase separation and gene control. *Science* **361**, eaar3958 (2018).
98. Plys, A. J. et al. Phase separation of polycomb-repressive complex 1 is governed by a charged disordered region of CBX2. *Genes Dev.* **33**, 799–813 (2019).
99. Tatavosian, R. et al. Nuclear condensates of the polycomb protein chromobox 2 (CBX2) assemble through phase separation. *J. Biol. Chem.* **294**, 1451–1463 (2019).
100. Melters, D. P., Paliulis, L. V., Korf, I. F. & Chan, S. W. L. Holocentric chromosomes: convergent evolution, meiotic adaptations, and genomic analysis. *Chromosome Res.* **20**, 579–593 (2012).
101. Stroustrup, N. et al. The *Caenorhabditis elegans* lifespan machine. *Nat. Methods* **10**, 665–670 (2013).

Publisher's note Springer Nature remains neutral with regard to jurisdictional claims in published maps and institutional affiliations.

Springer Nature or its licensor (e.g. a society or other partner) holds exclusive rights to this article under a publishing agreement with the author(s) or other rightsholder(s); author self-archiving of the accepted manuscript version of this article is solely governed by the terms of such publishing agreement and applicable law.

© The Author(s), under exclusive licence to Springer Nature America, Inc. 2024

Methods

Creation of TEV cleavage sites in individual kleisins and degron tagging of SDC-3

TEV cleavage sites were integrated into kleisin subunits of the different SMC complexes using clustered regularly interspaced short palindromic repeats (CRISPR)–Cas9 genome engineering[102], using *unc-58* or *dpy-10* co-CRISPR as marker. Similarly, *sdc-3* was modified amino terminally by integrating the degron sequence in frame with the protein in the HW2079 strain (kindly provided by H. Grosshans) expressing the TIR1 ubiquitin ligase under the control of the *eft-3* promoter. Template primers and guide RNAs are described in Supplementary Table 1.

Phenotypic characterization

Animals synchronized at the L1 stage were grown at 22 °C on fresh nematode growth medium (NGM) plates seeded with OP50-1 bacteria. After 3 h, the animals were heat shocked at 34 °C for 30 min and incubated at 22 °C for the rest of the experiment, while they were imaged and their phenotype quantified. Experiments were carried out at least twice.

Western blotting of TEV cleavage

Approximately 80,000 L1 stage-synchronized worms were grown on 150-mm NGM plates and heat shocked as described above. L3 stage worms were collected and washed 3× with M9, and the worm pellet was frozen at −80 °C. Pellets were defrosted and resuspended in 1 ml of 1× NPB buffer (20 mM Hepes, pH 7.6, 20 mM KCl, 3 mM $MgCl_2$ and 0.5 M sucrose) supplemented with protease inhibitors and 1 mM dithiothreitol. The worms were fragmented in a Balch homogenizer (Isobiotec) using 35 strokes with the 10-µm ball and combined with two rinses of the homogenizer with 0.75 1× NPB buffer. Fragmented worms were collected by centrifugation at 3,200*g* for 5 min at 4 °C. An equal volume of 2× sodium dodecylsulfate (SDS)–NaCl buffer (50 mM Tris, 2% SDS, 0.5 M NaCl) was added to the pellet and samples were boiled for 5 min, followed by sonication in a Bioruptor machine (Diagenode) for 10 min, set on high, 30 s on, 30 s off. Insoluble material was removed from the lysate by centrifugation for 5 min at room temperature (RT) and 5,000*g*. For one batch of worms, 15,000 worms were treated ± heat shock as above and, when collected, they were directly lysed in 2× Laemmli buffer without Balch homogenization, before being boiled and sonicated as above. Samples were run on 4–12% ExpressPlus poly(acrylamide) gel electrophoresis gels with Tris–3-(*N*-morpholino)propanesulfonic acid–SDS running buffer (GenScript). Transfer was carried out in the cold room overnight in Tris–glycine buffer (250 mM Tris, 1.92 M glycine and 10% ethanol) at 45 mA/30 V on to a nitrocellulose membrane. The 3× FLAG-tagged kleisins from strains PMW1005(*dpy-26*^{cs}), PMW1023 (*kle-2*^{cs}), PMW1021 (*scc-1*^{cs}) and PMW1025 (*coh-1*^{cs}) were detected using the mouse monoclonal anti-flag M2 antibody (Sigma-Aldrich, cat. no. F1804). The heat-shock-inducible, myc-tagged TEV protease was detected with a mouse monoclonal anti-myc antibody (Sigma-Aldrich, cat. no. M4439). The proteins were detected using SuperSignal West Femto Maximum Sensitivity Substrate (Thermo Fisher Scientific) and an Amersham Imager 600. The signals were quantified using ImageJ. For one blot where quantification was carried out for KLE-2 using a different exposure time, its signal intensity was normalized by the difference in the length of exposures. In all cases, band intensity was first normalized to the housekeeping gene tubulin (mouse anti-tubulin, Sigma-Aldrich, cat. no. T9026) and then, to compare between blots, signals were normalized either to COH-1 present on the same blot or by normalizing heat-shocked samples to nonheat-shocked samples.

Microscopy of SMC-1::GFP

TEV-only control (PWM941), cohesin$^{SCC\text{-}1/COH\text{-}1}$ (PMW947), cohesin$^{SCC\text{-}1}$ (PMW948) and cohesin$^{COH\text{-}1}$ (PWM949) strains, expressing endogenously GFP-tagged SMC-1 (ref. 51), were treated with and without heat shock at the L1 stage and imaged at the L3 stage on a Nikon Ti2 Crest spinning disk microscope. Fluorescence was quantified only from images of the head to avoid interference from the germline and autofluorescence in the gut. The head region was outlined manually in FIJI, along with a nearby background region on each image. Customized scripts in FIJI, Python and R (https://github.com/CellFateNucOrg/MoushumiDas_paper/tree/v0.4.1) were used to quantify the mean fluorescence intensity in the head and subtract the mean background intensity from the same image. Data from three separate experiments were combined for Supplementary Fig. 1d.

Quantification of seam cell divisions

To evaluate the progression of seam cell division, strains with TEV sites in kleisins expressing a fluorescent seam cell marker (wls[scm::gfp] V) were treated as above and the number of seam cells per animal was counted every 24 h for the next 3 d.

RNA-seq

For strains PMW366, PMW382, PMW775, PMW784, PMW828 and PMW844, synchronized L1 stage nematodes were seeded on to NGM plates and incubated for 3 h at 22 °C. The animals were heat shocked at 34 °C for 30 min to activate the TEV protease and incubated again for 19 h at 22 °C. For strains PMW821, PMW823 and PMW822, synchronized L1 stage nematodes were seeded on to NGM plates with 1 mM auxin (prepared in ethanol). As a control, the strain PMW822 was seeded on to NGM plates without auxin but with ethanol. L1 stage worms were incubated for 3 h at 22 °C, heat shocked at 34 °C for 30 min and incubated for another 19 h at 22 °C. At that stage, most of the population reached the L3 stage. Animals were washed 3× with M9 buffer. RNA was isolated from the worms using TRIzol, treated with DNase and cleaned using RNeasy MinElute Cleanup Kit. Sequencing libraries were created using the Illumina Stranded mRNA preparation kit. Libraries were sequenced on an Illumina Novaseq 6000 device at the NGS platform of the University of Bern.

RNA-seq data analysis

Between 37 and 60 million reads were generated from each library divided between two lanes of an Illumina NovaSeq 6000 machine. Adapters were trimmed with Cutadapt v.2.5, and reads were aligned to the WS275 version of the *C. elegans* protein-coding transcriptome using Salmon v.1.5.2 in quant mode with –seqBias –gcBias and --numBootstraps 100 options. Differential expression analysis was carried out with DESeq2 v.1.34. First, all genes with fewer than ten reads in total among all samples were removed. The cleavage of each of the kleisin subunits was contrasted with the control strain expressing only the TEV protease, while accounting in the design formula for variation arising from sequencing lane, biological replicate and sequencing date. The LFC estimates were shrunken using the 'apeglm' algorithm. An initial check showed that 35.1%, 51.5% and 49.6% of the significantly changing genes on cleavage of DPY-26, KLE-2 and SCC-1, respectively, were genes that oscillate during larval development[103,104]. Oscillating genes could produce a large fold-change in expression due to very small developmental asynchronies; therefore, we filtered out a combined list of 4,522 genes that oscillate during larval development from the DEseq2 object before analysis. Basic processing of the RNA sequencing (RNA-seq) data and exploratory data analysis were carried out with customized scripts in bash and R, which can be found on github (https://github.com/CellFateNucOrg/SMC_RNAseq/tree/v0.3). The scripts used to generate the figures in this paper can be found at https://github.com/CellFateNucOrg/MoushumiDas_paper/tree/v0.4.1. Significantly misregulated genes were filtered with an adjusted P (P_{adj}) value <0.05 and we considered either all statistically significant genes or those that also had an absolute LFC > 0.5, as indicated in the figure legends. This threshold was chosen empirically to maximize the number of significant X-linked genes on cleavage of DPY-26 while minimizing the number of autosomal genes that were considered significant.

RNA-seq was performed in strains containing SDC-3 tagged with the auxin-inducible degron tag and TIR1 ubiquitin ligase with and without auxin, as described in Supplementary Table 5. For better comparison to previous samples, all strains contained the heat-shock-inducible TEV protease and were heat shocked at the L1 stage. Mapping and differential gene expression analysis was performed with Salmon and DESeq2 as described above. DESeq2 analysis was carried out by creating a dummy variable containing all combinations of *dpy-26*^{cs}, *sdc-3*^{AID}, TIR1 and auxin treatment that were present in the data and initially all strains were compared with the PMW366 control strain without auxin, taking into account sequencing lane, biological replicate and sequencing date as control variables. More complex comparisons were carried out in DESeq2 to remove the background effects of auxin and TIR1 by subtracting the coefficients of the different levels of the dummy variable. In the results, we focused on the contrasts between PMW382 and PMW366 without auxin for *dpy-26*^{cs} effects and on the PMW822 strain with and without auxin for SDC-3 degron effects.

Lifespan assay

Animals were synchronized at the L1 stage and heat shocked as above. When they reached the L4 stage, they were transferred to tight-fitting plates (BD Falcon Petri Dishes, 50 × 9 mm^2) containing 50 mM fluorodeoxyuridine (FUdR) and permanently shifted to 20 °C. For degron-mediated degradation of SDC-3, *sdc-3*^{AID}, half of the animals were transferred to FUdR plates with 1 mM auxin diluted in dimethyl sufoxide (DMSO), whereas the other half were transferred to FUdR plates with DMSO as a control. Plates were then loaded into air-cooled Epson V800 scanners and imaged with a frequency of 2 scans per h using the lifespan machine setup[101]. The temperature of the scanner flatbed was continuously monitored (Thermoworks). Animals that exploded, burrowed or escaped the imaging area were censored. For data processing, L4 stage animals were defined as day 0 of adulthood. The Kaplan–Meier product-limit procedure, followed by the null hypothesis test employing the Mantel–Cox log(rank) approach, was applied to derive the survival function estimates. The survival data were processed in R using packages survminer (v.0.3.1) and survival (v.3.1-12).

Male lifespans are difficult to carry out on plates because the animals tend to crawl off and die. To overcome this difficulty, mixed populations were bleached, hatched and heat shocked as above and, after 2 d at 20 °C, 25 males were manually picked into 96 U-well microplates containing 100 µl of S-basal with 5× concentrated *Escherichia coli* per well, with 8 wells per strain as technical replicates. Healthspan assays were performed using wMicroTracker ONE (cat. no. MTK100) from InVivoBiosystems. Activity per well was measured once every 2 d until day 12 of adulthood and on a daily basis afterward. Each measurement included 3× 30-min periods, with a 1-min resolution. The motility rate of these periods was averaged between technical replicates for each strain. The experiment was repeated (biological replicates) and performed until reaching <5% of starting motility rates in both conditions. Contaminated wells were excluded from the analysis. Data were analyzed using GraphPad Prism 8 software.

Construction of Hi-C libraries

The 3D chromatin conformation was acquired as in ref. 47, using synchronized animals 19 h after heat shock for TEV induction as described above and with the following modifications. Animals were pelleted and stored at −80 °C. For fixation, the frozen worm pellet was resuspended in 2% formaldehyde prepared in M9 buffer and incubated for 30 min in the rotator. Formaldehyde was then quenched with glycine at 125 mM (final) and incubated for 5 min. The worms were pelleted again, washed with M9 and about 100 µl of the packed animals was transferred to a 1.5-ml microcentrifuge tube, washed with 1 ml of 1× phosphate-buffered saline (PBS) and protease inhibitors, washed again with 1 ml of 1× PBS and snap-frozen in liquid nitrogen before storage at −80 °C. Crosslinked frozen worms were ground using a SPEX6775 freezer/mill (SPEX Europe) at 5 cycles per s for 1 min with a total of 2 cycles. The ground worm powder was dissolved in 5 ml of 1× PBS and immediately crosslinked with 500 µl of TC buffer (100 mM NaCl, 1 mM EDTA, 0.5 mM (ethylenebis(oxonitrilo))tetra-acetate, 50 mM Hepes, pH 8.0, 22% formaldehyde), to a final concentration of 2% formaldehyde for 20 min at RT. Crosslinking was stopped by the addition of 289 µl of Stop Solution 1 (provided in the Arima Hi-C kit) and a 5-min incubation at RT. Samples were pelleted at 2,000*g* for 15 min at RT and resuspended in 5 ml of 1× PBS before 10 aliquots were distributed into 1.5-ml microcentrifuge tubes. The amount of DNA acquired from a single aliquot was estimated and, accordingly, the subsequent Hi-C experiment was done as per the manufacturer's instructions. For library preparation, the modified protocol from Arima Genomics for the KAPA Hyper Prep Kit was used. The libraries were sequenced with Illumina sequencing to generate 100-bp paired-end reads. Sequence data are presented in Supplementary Table 3 and available from Gene Expression Omnibus (GEO; accession no. GSE199723).

Hi-C data analysis

Hi-C Illumina data were processed using the HiCPro pipeline[105]. A Singularity container containing v.3.0.0 of HiCPro was run with customized bash scripts with default parameters in the config file, except for customization to the local cluster environment and the following parameters: BIN_SIZE = 2000, LIGATION_SITE = GATCGATC, GANTGATC, GANTANTC, GATCANTC for samples prepared with the Arima Hi-C kit, and using the ce11 genome downloaded from University of California, Santa Cruz (UCSC). The HiCPro results matrix was converted to cool format using the hicpro2higlass.sh tool from the Hic-Pro utils scripts. We then generated both balanced and unbalanced mcool files with our own customized resolutions (2,000, 4,000, 6,000, 8,000, 10,000, 20,000, 50,000, 100,000, 200,000 and 500,000 bp) with the cooler software (v.0.8.6) so that they could be viewed in HiGlass. The customized bash scripts can be found at https://github.com/CellFateNucOrg/hicpro/tree/v0.2. Additional data analysis was conducted with cooltools[106], GENOVA[107–111] and ad-hoc R scripts. For the conversion from eigenvector values to eigenvector value bins, the range of T/C or A/B eigenvector values (E1 or E2) determined for each genomic interval was split into 50 bins of equal genomic representation, and a bin value was assigned to each genomic interval, such that the lowest 2% of eigenvector values would get a bin value of 1 and the top 2% a bin value of 50. Spearman's correlation of eigenvalues with expression data shown in Fig. 2c was carried out using all 2-kb regions with transcripts per million (TPM) > 0. For three-way contacts analysis, forward and reverse reads that did not align in the first round of 'global' alignment of HiCPro were fused together in vitro and processed using the MC-HiC pipeline[65], with a 50-kb bin size and the bowtie2 mapper with parameters --very-sensitive -L 20 --re-min L,-0.6,-0.2 --end-to-end.

Reporting summary

Further information on research design is available in the Nature Portfolio Reporting Summary linked to this article.

Data availability

RNA-seq and Hi-C data have been submitted to the GEO, accession no. GSE199723. Source data are provided with this paper.

Code availability

Code has been deposited on GitHub and archived on Zenodo. The customized scripts to run the HiCPro pipeline are available at https://github.com/CellFateNucOrg/hicpro/releases/tag/v0.3 and https://doi.org/10.5281/zenodo.11536522 (ref. 112). The pipeline for data processing with salmon and DESeq2 is from https://github.com/CellFateNucOrg/SMC_RNAseq/tree/v0.4 and https://doi.org/10.5281/zenodo.11536434 (ref. 113). The scripts used to generate the RNA-seq and SMC-1 microscopy quantification figures in this paper are from

https://github.com/CellFateNucOrg/MoushumiDas_paper/tree/v0.4.1 and https://doi.org/10.5281/zenodo.11536430 (ref. 114).

References

102. Paix, A. et al. Scalable and versatile genome editing using linear DNAs with microhomology to Cas9 Sites in *Caenorhabditis elegans*. *Genetics* **198**, 1347–1356 (2014).
103. Latorre, I. et al. The DREAM complex promotes gene body H2A.Z for target repression. *Genes Dev.* **29**, 495–500 (2015).
104. Meeuse, M. W. et al. Developmental function and state transitions of a gene expression oscillator in *Caenorhabditis elegans*. *Mol. Syst. Biol.* **16**, e9498 (2020).
105. Servant, N. et al. HiC-Pro: an optimized and flexible pipeline for Hi-C data processing. *Genome Biol.* **16**, 259 (2015).
106. Venev, S. et al. open2c/cooltools: v0.4.1. *Zenodo* https://doi.org/10.5281/zenodo.5214125 (2021).
107. van der Weide, R. H. et al. Hi-C analyses with GENOVA: a case study with cohesin variants. *NAR Genom. Bioinform.* **3**, lqab040 (2021).
108. Kerpedjiev, P. et al. HiGlass: web-based visual exploration and analysis of genome interaction maps. *Genome Biol.* **19**, 125 (2018).
109. Yang, T. et al. HiCRep: assessing the reproducibility of Hi-C data using a stratum-adjusted correlation coefficient. *Genome Res.* **27**, 1939–1949 (2017).
110. Lin, D., Sanders, J. & Noble, W. S. HiCRep.py: fast comparison of Hi-C contact matrices in Python. *Bioinformatics* **37**, 2996–2997 (2021).
111. Angeles-Albores, D., Lee, R., Chan, J. & Sternberg, P. Two new functions in the WormBase Enrichment Suite. *microPubl. Biol.* https://doi.org/10.17912/W25Q2N (2018).
112. Semple, J. CellFateNucOrg/hicpro: final publication version for Zenodo. *Zenodo* https://doi.org/10.5281/zenodo.11536522 (2024).
113. Semple, J. & Das, M. CellFateNucOrg/SMC_RNAseq: final publication version for Zenodo. *Zenodo* https://doi.org/10.5281/zenodo.11536434 (2024).
114. Semple, J. CellFateNucOrg/MoushumiDas_paper: final publication version for Zenodo. *Zenodo* https://doi.org/10.5281/zenodo.11536430 (2024).

Acknowledgements

We thank C. Elcin and M. Berger for technical help, L. Giorgetti, S. Gasser, J. de Ridder, A. Allahyar and A. Gonzalez for discussions and optimizations of the project, P. Nicholson and her team at the NGS platform of the University of Bern, Meister laboratory for discussions and K. von Unen and the Pertz laboratory for help with HiLo microscopy. Some strains were provided by the Caenorhabditis Genetics Center, which is funded by National Institutes of Health Office of Research Infrastructure Programs (grant no. P40 OD010440). This work was funded by the Swiss National Science Foundation (grant nos 176226/PP00P3_159320 to P.M. and 190072 to C.Y.E.), the University of Bern, the SBFI ESKAS Program 2020.0321 (to V.V.) and the Novartis Foundation for Medical/Biological Research (to P.M.).

Author contributions

M.D., J.I.S., A.H., J.S., J.C. and P.M. constructed the *C. elegans* strains used in the present study, including both the TEV protease and auxin-inducible degradation system. The phenotypic assay was done by M.D. and the seam cell counting by A.H. J.I.S. performed western blotting. Lifespan assays were carried out by C.S., A.D. and C.Y.E. A.H., V.V., J.I.S. and J.S. were all involved in capturing the microscopic images. M.D. optimized and performed the Hi-C and RNA-seq experiments. J.I.S., T.G., M.D., J.M. and P.M. performed the bioinformatic analyses of the Hi-C and RNA-seq datasets. A.A. performed the exon–intron split analysis. M.D., J.I.S. and P.M. were involved in interpretation of the data and writing the paper. P.M. supervised the study.

Competing interests

The authors declare no competing interests.

Additional information

Supplementary information The online version contains supplementary material available at https://doi.org/10.1038/s41588-024-01832-5.

Correspondence and requests for materials should be addressed to Peter Meister.

Peer review information *Nature Genetics* thanks the anonymous reviewers for their contribution to the peer review of this work.

Reprints and permissions information is available at www.nature.com/reprints.

nature portfolio

Corresponding author(s): Meister, 63304

Last updated by author(s): Jun 9, 2024

Reporting Summary

Nature Portfolio wishes to improve the reproducibility of the work that we publish. This form provides structure for consistency and transparency in reporting. For further information on Nature Portfolio policies, see our Editorial Policies and the Editorial Policy Checklist.

Statistics

For all statistical analyses, confirm that the following items are present in the figure legend, table legend, main text, or Methods section.

n/a	Confirmed	
☐	☒	The exact sample size (*n*) for each experimental group/condition, given as a discrete number and unit of measurement
☐	☒	A statement on whether measurements were taken from distinct samples or whether the same sample was measured repeatedly
☐	☒	The statistical test(s) used AND whether they are one- or two-sided *Only common tests should be described solely by name; describe more complex techniques in the Methods section.*
☐	☒	A description of all covariates tested
☐	☒	A description of any assumptions or corrections, such as tests of normality and adjustment for multiple comparisons
☐	☒	A full description of the statistical parameters including central tendency (e.g. means) or other basic estimates (e.g. regression coefficient) AND variation (e.g. standard deviation) or associated estimates of uncertainty (e.g. confidence intervals)
☐	☒	For null hypothesis testing, the test statistic (e.g. *F*, *t*, *r*) with confidence intervals, effect sizes, degrees of freedom and *P* value noted *Give P values as exact values whenever suitable.*
☒	☐	For Bayesian analysis, information on the choice of priors and Markov chain Monte Carlo settings
☐	☒	For hierarchical and complex designs, identification of the appropriate level for tests and full reporting of outcomes
☐	☒	Estimates of effect sizes (e.g. Cohen's *d*, Pearson's *r*), indicating how they were calculated

Our web collection on statistics for biologists contains articles on many of the points above.

Software and code

Policy information about availability of computer code

Data collection	Illumina Novaseq 6000 device for HTS with proprietary Illumina basecalling software, RTA v3.4.4, bcl2fastq v2.20.0.422
Data analysis	Custom RNA-seq pipeline https://github.com/CellFateNucOrg/MoushumiDas_paper/releases/tag/v0.4.2; DOI 10.5281/zenodo.11536430; https://github.com/CellFateNucOrg/SMC_RNAseq/releases/tag/v0.4 DOI 10.5281/zenodo.11536434; HiC-Pro pipeline https://github.com/CellFateNucOrg/hicpro/releases/tag/v0.3; DOI 10.5281/zenodo.11536522 cooltools v0.5.0 cooler v0.8.10 HiGlass-docker v0.10.4 hicrep v0.2.6 Custom HiC scripts using GENOVA https:/ /github.com/robinweide/GENOVA

For manuscripts utilizing custom algorithms or software that are central to the research but not yet described in published literature, software must be made available to editors and reviewers. We strongly encourage code deposition in a community repository (e.g. GitHub). See the Nature Portfolio guidelines for submitting code & software for further information.

Data

Policy information about availability of data

All manuscripts must include a data availability statement. This statement should provide the following information, where applicable:

- Accession codes, unique identifiers, or web links for publicly available datasets
- A description of any restrictions on data availability
- For clinical datasets or third party data, please ensure that the statement adheres to our policy

RNA-seq and Hi-C data has been submitted to GEO GSE199723, made public April 17th, 2024

Research involving human participants, their data, or biological material

Policy information about studies with human participants or human data. See also policy information about sex, gender (identity/presentation), and sexual orientation and race, ethnicity and racism.

Reporting on sex and gender	N/A
Reporting on race, ethnicity, or other socially relevant groupings	N/A
Population characteristics	N/A
Recruitment	N/A
Ethics oversight	N/A

Note that full information on the approval of the study protocol must also be provided in the manuscript.

Field-specific reporting

Please select the one below that is the best fit for your research. If you are not sure, read the appropriate sections before making your selection.

☒ Life sciences ☐ Behavioural & social sciences ☐ Ecological, evolutionary & environmental sciences

For a reference copy of the document with all sections, see nature.com/documents/nr-reporting-summary-flat.pdf

Life sciences study design

All studies must disclose on these points even when the disclosure is negative.

Sample size	All samples sizes for phenotypic scoring (Figure 1) are indicated in the corresponding panel. Every bulk sequencing-based experiment (HiC, RNA-seq) has been performed twice on independent biological samples. Each imaging experiment has been performed at least twice. Lifespan number of animals are indicated in supplementary table 4, and performed in triplicates.
Data exclusions	One RNA-seq sample was excluded as it was an outlier (replicate 3 from KLE-2 cleavage, mentioned in the methods section)
Replication	All HiC experiments were performed twice (biological replicates). All RNA-seq experiments were made in triplicates at least. All microscopy experiments were performed at least twice.
Randomization	No randomization
Blinding	No blinding

Reporting for specific materials, systems and methods

We require information from authors about some types of materials, experimental systems and methods used in many studies. Here, indicate whether each material, system or method listed is relevant to your study. If you are not sure if a list item applies to your research, read the appropriate section before selecting a response.

Materials & experimental systems

n/a	Involved in the study
☐	☒ Antibodies
☒	☐ Eukaryotic cell lines
☒	☐ Palaeontology and archaeology
☐	☒ Animals and other organisms
☒	☐ Clinical data
☒	☐ Dual use research of concern
☒	☐ Plants

Methods

n/a	Involved in the study
☒	☐ ChIP-seq
☒	☐ Flow cytometry
☒	☐ MRI-based neuroimaging

Antibodies

Antibodies used

Monoclonal mouse anti-FLAG M2 Sigma F1804
Monoclonal mouse anti-tubulin clone DM1A, Sigma T9026
Monoclonal mouse anti-c-Myc clone 9E10, Sigma M4439

Validation

Commercial antibodies against affinity epitopes, validated by the manufacturer
https://www.sigmaaldrich.com/deepweb/assets/sigmaaldrich/product/documents/119/160/f1804bul-mk.pdf
https://www.sigmaaldrich.com/deepweb/assets/sigmaaldrich/product/documents/657/361/t9026blot.pdf
https://www.sigmaaldrich.com/deepweb/assets/sigmaaldrich/product/documents/254/684/m4439pis-mk.pdf

Animals and other research organisms

Policy information about studies involving animals; ARRIVE guidelines recommended for reporting animal research, and Sex and Gender in Research

Laboratory animals

C. elegans nematodes, L3 stage for HiC/RNA-seq, range of different ages for the phenotypic characterization (from L1 to adults)

Wild animals

No wild animals were observed or captured for this study.

Reporting on sex

Only hermaphrodite animals were used, except for Figure 1h, where the healthspan of male animals (non-dosage compensated) was measured.

Field-collected samples

No field-collected samples were used in this study.

Ethics oversight

No ethical approval or guidance was required - research work with nematodes.

Note that full information on the approval of the study protocol must also be provided in the manuscript.

Plants

Seed stocks

N/A

Novel plant genotypes

N/A

Authentication

N/A